ECLIPSE MAPPING OF ACCRETION DISKS IN CATACLYSMIC BINARIES

Thesis by

Keith Douglas Horne

In Partial Fulfillment of the Requirements
for the Degree of
Doctor of Philosophy

California Institute of Technology
Pasadena, California

1983

(Submitted January 7, 1983)

To the Memory of

Peter J. Young

ACKNOWLEDGEMENTS

The foundation on which this thesis rests has been laid primarily by a group of people in Cambridge, England whose efforts have greatly advanced the development of maximum entropy imaging over the last five years. I especially wish to thank Stephen Gull, who kindly made available to me a copy of the maximum entropy program MEMSYS, and John Skilling, whose Laramie review paper so beautifully explains the workings of MEM.

Jim Pringle is responsible for my initial interest in accretion disks in close binaries, and Richard Wade deserves much credit for stimulating that interest on many occasions over the years. I am grateful to Bev Oke for his humility and generosity as an advisor and to many other people at Caltech from whom I have learned so much. I have been privileged to share observing collaborations with Rae Steining and with Richard Gomer, whose high-speed photometer data systems permitted observations of a kind not normally conducted at Caltech which were essential to this thesis work. I am additionally grateful to Richard Gomer for many years of continual friendship and for his services on numerous occasions as my lawyer.

A large debt is owed to a great many persons who have invested time and energy in developing the Caltech/JPL Astronomy computing facilities. Special thanks belong to Tim Pearson, Marty Ewing, Kimo Yap, Dan (The Great Zar)

Zirin, Judy Cohen, and Mike Lesser. This thesis would not have been possible with the computing facilities available here only a few years ago.

I am grateful to the Astronomy department for providing travel assistance which enabled me to attend several workshops and conferences during my graduate years. These meetings served as occasions for broad reflection and provided rewarding contact and productive collaboration with scientists outside the Caltech community. I pray that the recent trend toward reduction of this valuable form of support to Caltech Astronomy graduate students will soon be reversed.

Best wishes to all of my fellow occupants of the lower levels of Robinson. To Matt, Don, Alex, John, Mike, Abi, Bruce, James, George, Fred, Dave, Alain, Roger, Steve, Tex, Jeff, Ken, Raghvendra, Dean, Kwok, and Michael (why are none of you women?), your comraderie and companionship will be warmly remembered and sorely missed.

ABSTRACT

Surface brightness distributions for accretion disks in eclipsing cataclysmic binaries may be reconstructed from observed eclipse light curves by use maximum entropy imaging methods. Three-color eclipse photometry of six eclipsing cataclysmic binaries provides the basis for an observational study of the local and global structure of their accretion disks. Observations from several eclipse cycles are averaged to form mean eclipse profiles with diminished contamination by flickering. Flickering is shown to be widely distributed over the face of the accretion disks in RW Tri and LX Ser. Accretion disk maps are derived which give satisfying fits to the observed eclipse profiles and which are maximally symmetric about the center of the disk. Disk maps for nova DQ Her and for four nova-like systems show broad intensity distributions with bright spots, associated with the gas streams that feed the disks, in evidence at a radii comparable to the disk tidal radius. The HT Cas disk is smaller and is dominated by a compact source at its center. Analysis of disk intensity maps at U, B and R show that the brighter parts of the accretion disks are optically-thick thermal radiators with temperatures which decrease with radius. The angular scale of each disk is fixed by a method analogous to cluster main sequence fitting. Distance estimates are derived which are free of assumptions about the global structure of the disks, but which depend on currently uncertain dyamical parameters of the binaries. The temperature in the disk is observed to fall much more slowly with radius than the $R^{-3/4}$ law predicted by a steady-state mass-conserving viscous accretion disk model. Apparently, much of the visible light from the disk is produced by reprocessing of hard radiation from the center of the disk. Upper limits are found for the mass transfer rates which are one to two orders of magnitude smaller than the canonical mass transfer rate for novae and nova-like systems and which thus are in better agreement with mass transfer driven by gravitational radiation alone. Mass transfer rates have previously been systematically overestimated by the neglect of reprocessing. The accretion disk in HT Cas is shown to be optically thin in the Paschen continuum. The compact bright source at the center of its disk is a composite of light from the photosphere of the white dwarf and of free-free emission from hot gas in the accretion boundary layer.

TABLE OF CONTENTS

I. INTRODUCTION

Accretion disks occur in a diverse variety of astrophysical settings. Quasars and active galactic nuclei may be powered by the release of gravitational potential energy as gas is fed to a massive black hole by an accretion disk. Many of the x-ray sources within our galaxy are identified with binary star systems in which an accretion disk forms around a neutron star from matter lost by its companion star. Viscous stresses in accretion disks provide a means of removing the angular momentum of material collapsing to form new stars. Our own planetary system may be the remnant of an accretion disk which once surrounded young Sol.

The best astrophysical laboratories currently available for the study of accretion disks are the cataclysmic variables. These are close binary star systems, with orbital periods ranging from 80 minutes to around 12 hours, in which material lost from a cool dwarf star feeds an accretion disk around a white dwarf. The luminosity of these systems is provided largely by the release of gravitational energy as gas in the disk spirals inward toward the white dwarf. For a dozen or so of the known cataclysmic variables, deep eclipses have been found to occur as the red dwarf star passes in front of the accretion disk. The shape of the eclipse profile harbors information, albeit in convolved form, about the spatial structure of the disk.

This paper develops a method which may be used to reconstruct the accretion disk surface brightness distribution from the shape of an observed eclipse profile and presents the first observational study of the spatial structure of disks. Three-color photometry of accretion disk eclipses in six cataclysmic binaries is presented in Section II. Section III develops the maximum entropy techniques that are applied to this data to derive maps of the spatial brightness distributions of six accretion disks at each of three wavelengths. Section IV begins with a local analysis of the maps which serves to identify emission mechanisms and provides distance estimates and then proceeds to an investigation of the global structure of the disks and comparison with the standard viscous accretion disk model. Section V summarizes the current results and concludes with a discussion of prospects for the new eclipse mapping technique.

II. ECLIPSE OBSERVATIONS

Three-color photometry of eclipsing cataclysmic binaries was acquired during 1982 June 18-28 with the NASA/University of Arizona 1.5-m telescope at Mt. Lemmon and during 1982 Sept 15-23 with the Caltech/Carnegie 1.5-m telescope at Palomar Mountain. The systems under study here include the eclipsing dwarf nova HT Cas, observed while in its quiescent state, nova DQ Her (1934), and the nova-like variables RW Tri, UX UMa, LX Ser (Stepanyan's star) and Lanning 10. The observations, summarized in Table 1, consist of between two and six eclipse runs for each of these systems. Most of the eclipse runs cover at least the binary phase range (-0.2,0.2) intended to give ample baselines before and after each eclipse.

a) Instrumentation

The three-color photometer employed for these observations is a successor of the two-color instrument used by Hildebrand, Spillar and Stiening (1981). Simultaneous flux measurements in three spectral bandpasses were made by employing a pair of dichroic beam splitters to direct light to three photomultiplier tubes. Ultraviolet light incident at 45° on the first dichroic element is reflected through a 1 mm Schott UG5 filter to a Hammamatsu R670-04 photomultiplier tube. The second dichroic reflects blue light through a glass lens to a second R670-04 tube. The transmitted beam from the second dichroic passes through a Schott 115 infrared blocking filter, 3 mm of OG590 and a quartz lens to an RCA C31034 GaAs photomultiplier tube. Small photocathodes in the Hammamatsu tubes permitted their operation at ambient temperature without excessive dark count rates while the GaAs tube was cooled by dry ice. Response profiles taking into account the transmission of optical elements, photocathode sensitivities and one airmass atmospheric extinction are shown in Figure 1. These broad bandpasses, which resemble the corresponding Johnson standard bandpasses, will be loosely referred to as U, B, and R although the measurements are reduced directly to absolute fluxes, as described in Section IIIb, rather than to the Johnson system.

The photometer hardware used at Palomar included an additional quartz lens immediately behind the Cassegrain focal plane to reimage the diverging F/8.7 beam. Drift scan tests adequately demonstrated the constancy of the count rate for a standard star variously placed within the focal plane aperture. A 17 arcsecond diameter aperture was employed for all of the observations except those of HT Cas, for which an 11 arcsecond aperture was used. The telescope tracking was monitored and updated manually during the long eclipse runs by viewing an offset guide star visually at Mt.Lemmon or with the aid of an ISEC video camera and TV monitor at Palomar.

The high-speed data system, built around a Z80 micro-processor chip, supervised the counting of pre-amplified pulses from the three photomultiplier tubes. The internal data system clock, set to within 0.2 seconds of UTC by use of WWV time signals, provided a stable time base for the observations. Count rate samples averaged typically over 1 second intervals were stored in three 8192-sample memory buffers which at the end of each eclipse run were copied into files on 5.25-inch floppy diskettes. The data could later be read back into memory for graphic display as a light curve on an oscilloscope. A variable-pitch tone generator provided an audible real-time monitor of the count rate in one channel.

b) Data Reduction and Calibration

The raw data were processed on the Caltech Astronomy VAX 11/780's with an interactive reduction system. Each eclipse run consists primarily of observations of the eclipsing object under study, but includes in addition short observations of adjacent blank sky fields and of one or two reference stars distant from the object of interest by at most a few arc minutes. These various observations were conveniently segregated by an automatic routine which scanned the data stream to locate sudden changes in count rate which signal the transitions between fields. The occasional transition gradual enough to fool the automatic procedure was corrected manually in a second pass through the data.

The observations of blank sky fields, usually of 30-s duration, were always made at the beginning and end of each eclipse run and usually at several intermediate times which included one near mid-eclipse. The sky background (moon down) in the 17 arcsecond aperture contributed fluxes of 1.5, 3, and 6 milli-janskys to the U, B, and R bandpasses, while fluxes from the eclipsing objects ranged from 1 to 27 milli-janskys out of eclipse and from 0.15 to 11 milli-janskys during eclipse. (A milli-jansky corresponds to magnitude AB=16.4) A spline fit interpolated the background count rate measurements with an estimated maximum error of several percent.

Light from the nearby reference star, metered at two to five times during each eclipse run, served as a monitor of the atmospheric extinction. Following sky subtraction, the mean count rate for each reference star observation and for observations of additional flux-calibration objects were extracted from the data and analyzed by least squares to determine the effective extinction per airmass for each bandpass. A single set of extinction coefficients adequately represented the extinction data from the Mt. Lemmon run, while the Palomar data showed the extinction to vary vary from night to night at the level of 0.05 magnitude per airmass. The variable extinction component was grey and therefore probably results from scattering by large particles possibly associated with recent volcanic eruptions in Mexico.

Color terms, which in broadband photometry of stars compensate for changes in the effective extinction with the spectrum of the object, are of dubious value here since the spectra of cataclysmic variables differ considerably from those of normal stars. The impact of their neglect is diminished by correcting the data for atmospheric extinction only to an airmass of 1 and thereby avoiding the long extrapolation from the airmass of the observations to airmass 0. All comparison with theoretical models will occur following a convolution of model spectra with the calculated bandpasses, which include one atmosphere of extinction.

Absolute flux calibration was accomplished through observations of the four subdwarf flux standards of Oke and Gunn (1982). For a few nights on which observations of the subdwarf standards were omitted, the photometry was reduced by using reference stars as secondary flux standards. The monochromatic flux distribution f(nu) of each subdwarf standard was averaged over log(λ) with the calculated filter response profiles (Figure 1) to obtain broadband AB79 magnitudes. The broadband AB79 magnitude of any object is that of a flat spectrum source (AB79 = constant) that, if observed through the broad bandpass, would produce a count rate identical to that produced by the object. Here AB79 = $-2.5 \log_{10}(\mathrm{ergs/cm^2/s/Hz}) - 48.60$ so that AB79(5500Å) is approximately the same as V, and a flux of 1 milli-jansky corresponds to AB79 = 16.4. Broadband magnitudes for the subdwarf standards, which define our photometric system, are tabulated in Table 2 along with the effective wavelength, r.m.s. width and effective atmospheric extinction for each bandpass. The latter quantities depend of course on the spectrum of the object observed, those listed being for the spectra of the subdwarf flux stars. Results given for V and I bandpasses are for future reference.

The observed count rates for the standard stars, after correction to the zenith, varied by roughly 5 percent over the course of each observing run. Several Kitt Peak IIDS flux standards were observed as a check on the absolute photometry. Their observed magnitudes agreed with those calculated from their spectrophotometry (AB69(λ)) to within 5 percent, and part of this discrepancy may be attributed to the differences between the AB69 and AB79 systems. The evidence suggests that systematic error in the absolute calibration of the eclipse observations does not exceed 5 percent, and may actually be as good as 3 percent.

c) Mean Eclipse Profiles

Superimposed on the profile of each individual eclipse run are the ubiquitous fluctuations in brightness, termed "flickering," which are characteristic of cataclysmic variables. Because flickering timescales overlap those present in the eclipse profile, the eclipse and flickering effects cannot be cleanly separated by time-series filtering techniques. Observations of several eclipses in the same system may instead be averaged to diminish the influence of flickering. Provided that gross differences do not occur among the individual eclipse profiles, the resulting mean eclipse profile represents the time-averaged behavior of the accretion disk and is therefore more suitable for comparison with theoretical accretion disk models.

In order to construct mean eclipse profiles, phase-binned light curves were formed by casting the flux samples from a given eclipse run onto a standard set of binary phase bins and averaging the flux samples falling into each bin. Bins spanning 5 milli-cycles were adequate to resolve all significant structure in the eclipse profile for every system but HT Cas, which required 2 milli-cycle bins at some phases. Mean eclipse profiles were then obtained by a direct averaging of the phase-binned light curves for all eclipse runs on a given system. As none of these averages involved observations in both June and September, the time interval over which the eclipse curves were averaged never exceeded one week.

Figure 2 shows the mean U, B, and R eclipse profiles obtained for the six systems in this study. Also given, for the B bandpass only, are curves showing the difference between each individual phase-binned light curve and the mean profile. A considerable reduction in the flickering noise has been achieved in the mean profiles of HT Cas, LX Ser and RW Tri. Residual flickering effects of order 0.05 magnitude, somewhat more in the case of HT Cas, are witnessed by irregularities of this size in portions of the mean light curve outside of the eclipse. The flickering in UX UMa appears to be of comparable amplitude, although only two eclipses of this system were observed. A sizable disparity is seen between the two observed eclipses of DQ Her, and only a single eclipse of Lanning 10 had sufficient phase coverage for the eclipse study.

With the exception of those for HT Cas, the mean eclipse profiles seen in Figure 2 share a common morphology. All have round bottoms indicating that the disks are not totally eclipsed by their companion lobe-stars. In all cases half or more of the U light visible outside of eclipse is absent at mid-eclipse suggesting, but not proving, that the center of the accretion disk is occulted in each case. The various observed eclipse widths reflect primarily differences in the eclipse geometry (the binary mass ratios and inclinations). None of the eclipses extends beyond 0.15 cycles from mid-eclipse, although the egress branch of the eclipse of HT Cas approaches this limit. Material occulted at such phases would lie outside the Roche lobe of the white dwarf. The HT Cas eclipse is further distinguished by two sudden brightness transitions which correspond to the ingress and egress of a bright compact source which Patterson (1981) identifies with the white dwarf. Disparity between the flux levels observed before and after the eclipse, particularly large for the U eclipse of RW Tri, will be commented on later.

The mean eclipse profiles exhibit an asymmetry in the sense that the decline in brightness prior to mid-eclipse occurs in a shorter time than does the subsequent recovery. An abrupt change in slope on the egress branch of the profile initiates a period of more gradual brightening, and a similar though less distinct effect may occasionally be discerned during ingress. The effect, most pronounced for Lanning 10 and UX UMa, is traditionally attributed to the eclipse of a "bright spot" associated with the impact shock between material falling from the inner Lagrangian point and the rim of the disk.

d) Flickering

The origin of the flickering seen in cataclysmic variables has not yet been thoroughly investigated. In the dwarf nova U Gem, a major component of the flickering apparently arises near the bright spot, since flickering ceases during the eclipse which covers the region around the spot but not the central parts of the disk (Warner and Nather 1971). Such flickering may be attributed to inhomogeneities in the gas stream. Patterson (1981) identifies the site of flickering in HT Cas with the compact bright source at the center of its disk. Here intermittent shocks may occur as material orbiting in the disk enters the atmosphere of the white dwarf. Thus at least two distinct mechanisms may be involved in the production of flickering.

Eclipses provide an important tool in the study of flickering which might be more thoroughly utilized in the future. In Figure 3 are shown RMS eclipse profiles representing the eclipse of the time-variable component of the light from the accretion disks in LX Ser and RW Tri. The RMS profiles are obtained by computing the standard deviation of the fluxes occurring at each phase of the individual eclipse profiles. The phase width and center of the RMS eclipse profile are similar in both cases to those of the corresponding mean eclipse profile, which suggests that flickering activity in these two nova-like systems is broadly distributed over the face of the disk in a manner similar to that of the time-averaged light. The errors in the RMS profiles remain large, however, as only 4 and 6 eclipse runs are available in the present study. In addition, both rapid flickering and longer-term variations caused by secular changes in the global structure of the disk are expressed in the RMS profiles of Figure 3. High-pass digital filtering could be used to isolate the high-frequency component and, with a large number of eclipses, the resulting RMS profile might be useful in mapping the spatial distribution of flickering on the face of the accretion disk in much the same way that the time-averaged light from the disk is mapped from the mean eclipse profile in Section III.

e) Color Variations

The complex spectral changes observed during the eclipses may be examined in the color-index curves of Figure 4. The spectral variations follow approximately a mirror symmetry about the phase of mid-eclipse, although significant deviations from exact symmetry do occur. In all systems, the B-R color index, which measures the slope of the Paschen continuum, becomes redder near mid-eclipse. This universal feature is centered at the time of mid-eclipse but spans a shorter phase range than does the eclipse as a whole. In four of the systems, B-R becomes slightly bluer during the early stages of the eclipse; the onset of the eclipse occurs earlier in the R band than it does at B. A similar effect, though less pronounced, occurs during egress. The U-B curves exhibit a wider variety of behavoir. Outside of eclipse, five of the six systems, the exception being HT Cas, display a Balmer jump in absorption (U-B > 0). U-B becomes bluer at mid-eclipse in four systems, redder in two, and reverses trend five times during the eclipse of RW Tri. Brief increases in Balmer emission may be noted immediately following the ingress and just prior to the egress of the white dwarf in HT Cas.

The color variations arise as different parts of the accretion disk pass out of view behind the red dwarf star, but variations in the integrated light are difficult to interpret directly and without ambiguity. For example, the observed reddening of B-R might be produced by light from the red dwarf star, from cool outer regions of the accretion disk that remain visible at mid-eclipse, from circumbinary material, or even from a faint field star located within the observing aperture. A decrease in U-B near mid-eclipse might result from Balmer continuum emission by optically thin material, but the optically thin material might lie in the outer annuli of the disk or in a circumbinary region. The occultation of material with a Balmer jump in absorption might also mimic the appearance of Balmer continuum emission. More powerful techniques like those developed in the following section are needed to interpret the complex behavior observed during the accretion disk eclipses.

III. ECLIPSE MAPS OF THE ACCRETION DISK

A great deal of information about the physical structure of the accretion disk is reflected in the shape of its eclipse light curve and in color changes during the eclipse. Unfortunately, the information is held in a highly convolved form, and special effort is required for its extraction. This explains, perhaps, why the problem has received so little attention since the early suggestion by Nather and Robinson (1974) that the asymmetric eclipse profile of UX UMa might be decomposed into a symmetric component due to the accretion disk and a bright spot component resembling the partial eclipse in U Gem.

Simple model fitting techniques may be of some use in interpreting eclipse light curves, but their value is diluted by the presence of conspicuous asymmetry in the observed light curves and the current limitation of theoretical disk models to the case of azimuthal symmetry. Unreliable conclusions might easily be drawn by fitting a symmetric disk model to the clearly composite eclipse light curves. Our experience with model fitting indicates that at best only crude fits to the observed light curves can be attained without the introduction of a prohibitively large number of parameters (see also Frank and King 1981 and Frank et al. 1981). Benefit may also be derived at this stage by retaining a more general context than that provided by specific accretion disk models since these are largely untested by observations.

In this section, model-independent techniques are developed which achieve satisfying fits to the observed eclipse profiles. After discussing numerical methods for simulating the accretion disk eclipse and maximum entropy mapping techniques, accretion disk maps will be derived from the eclipse observations described in Section II.

a) The Eclipse Model

The red dwarf star which occults the accretion disk is severely distorted by tidal interaction with its degenerate companion. The Roche potential, which includes the gravity of two point masses in a circular orbit and centripetal acceleration for material in synchronous rotation, describes to good approximation the forces acting on material near the surface of the red dwarf star. Spillover of material from the red dwarf star through the throat in the Roche potential at the inner Lagrangian point ensures that the surface of the star will lie close to the critical Roche equipotential surface. We assume that it fills its Roche lobe exactly. Calculations in the Roche geometry are performed numerically following the methods of Mochnacki (1971); we do not employ a spherical star approximation. We assume also that the disk is flat and lies in the binary orbit plane. The flat disk approximation certainly will fail for nearly edge-on disks ($i \rightarrow 90^\circ$). However, the opening angles of disks are expected to be at most a few degrees while eclipses can occur at quite modest inclinations ($i \sim 70^\circ - 75^\circ$) in the close binaries under consideration here.

A Cartesian grid divides the disk plane into N^2 cells (here $N = 51$) which collectively cover a square region concentric with the disk and bisected along one edge by the inner Lagrangian point. R_{L1}, the distance from the center of the disk to the inner Lagrangian point, is a natural unit of length for eclipse studies of accretion disks since in these units the white dwarf Roche lobe retains a radius near 0.8 over a broad range of binary mass ratios $q = M_r/M_w$. Each grid cell J covers an area $4\left[\frac{R_{L1}}{N}\right]^2$, and may be ascribed an intensity I(J). If the eclipse observations occur at specific binary phases $\phi(K)$, the corresponding predicted fluxes are given by a sum of contributions from each cell in the grid.

$$f(K) = \theta^2 \frac{4}{N^2} \sum_{J=1}^{N^2} I(J)\ O(J,K) \tag{1}$$

where $\theta^2 = \left[\frac{R_{L1}}{D}\right]^2 \cos(i)$ and D is the distance of the binary from Earth. Convenient units for the parameter θ, which sets the angular scale of the system, are solar radii per kiloparsec (4.65 micro-arcseconds).

The geometry of the eclipse is described by the occultation kernel O(J,K), which gives the fraction of disk element J that is visible from the earth at phase $\phi(K)$. These may simply take on the values 0 or 1 depending whether or not the center of the element is eclipsed, or more accurate values may be calculated by locating the edge of the occultation region more precisely along two edges of the grid element. To determine whether a particular point on the disk is eclipsed at a given phase, a ray is traced from the point in question toward the earth. The Roche potential is calculated at small intervals along the ray to discover whether the potential falls below the critical value which defines the occulting surface of the lobe-star. An efficient algorithm has been evolved to minimize the computation required to evaluate the occultation kernel completely.

b) Geometric Parameters

The eclipse geometry is completely specified by three parameters, the binary phase of conjunction ϕ_0, the phase width of the eclipse at the center of the disk $\Delta\phi$, and the mass ratio q. Since the occulting star fills its Roche lobe, a relation exists between q, $\Delta\phi$ and the inclination i (Figure 5). For systems in which the center of the disk is eclipsed, $\Delta\phi$ serves more adequately as a parameter than does the inclination since the value of the former is more directly constrained by the eclipse observations.

Since the observed eclipse depths exceed one magnitude in the U band, we may plausibly assume that the center of each accretion disk is occulted at mid-eclipse. The phases of steepest slope in the eclipse profile, which correspond approximately to ingress and egress of the brightest part of the disk, then provide estimates for $\Delta\phi$ and ϕ_0. Photometry also places a lower limit on the mass ratio q since the observed eclipse phase width will not be achieved even at 90° inclination for sufficiently small values of q (Figure 5). An upper limit may be set at $q = 1$ by the expectation that mass transfer will proceed on a dynamical timescale in low-mass systems with $q > 1$, quickly leading to the formation of a common-envelope binary (Paczynski 1971, Webbink 1977). Spectroscopic observations lead to further constraints on the mass ratio but generally fall short of adequately defining its value.

Orbital radial velocity amplitudes for both component stars are necessary to determine the masses of an eclipsing binary. The red dwarfs in eclipsing cataclysmic binaries are faint relative to the accretion disk and to date no radial velocity information is available for the red dwarf stars in the systems under study here. Emission lines from the accretion disk trace radial velocity curves that agree roughly with those expected for the white dwarf component, but the great breadth and asymmetric character of the line profiles cause a sensitive dependence on the method used to extract the velocities. Often a sizable (0.1 cycle) discrepancy between the phase of spectroscopic conjunction and the phase of the eclipse warns that the emission line velocities may inaccurately reflect the orbital motion of the white dwarf. Until these effects are understood -- calculations by Wade (1981) demonstrate that they cannot safely be ignored -- the emission line velocities must be used with some reserve, particularly when a phase offset is present.

The eclipse geometry is most secure in the case of HT Cas. The eclipse width and center are accurately defined by sharp transitions produced in the eclipse profile by the ingress and egress of a compact source presumed to lie at the center of the disk. A radial velocity curve from the wings of the strong double-peaked Balmer emission lines (Young, Schneider and Shectman 1981b) gives $K_{em} = 115$ km/s, but is offset some 0.09 cycles relative to the eclipse. With $K_w = 115$ km/s, the Chandrasekhar mass limit requires $q > 0.28$ and the maximum velocity (2820 km/s) in the emission line profile, if attributed to orbital motion near the surface of the white dwarf, requires $q < 0.34$. The permitted range shifts to $0.28 < q < 0.38$ if $K_w = 130$ km/s. A value near the upper end of this range is suggested by two independent arguments. First, the duration of the ingress and egress of the compact source will then imply for it a radius in agreement with that of a Hamada-Salpeter white dwarf (Patterson 1981). Second, the observed phase offsets between eclipses of line emission at different velocities will then be consistent with a Keplerian disk (Young, Schneider and Shectman 1981b). We adopt $q = 0.35$.

The four eclipses of LX Ser in this study occur early by 0.017 cycles relative to the ephemeris found by Horne (1980). The 0.081 cycle eclipse width requires $q > 0.22$. Radial velocity work by Young, Schneider and Shectman (1981a) gives $K_{em} = 160$ km/s, although again a phase offset of 0.09 cycles remains unexplained. Adopting $K_w = 160$ km/s, the Chandrasekhar limit requires $q > 0.47$ and the emission line velocity width $V_{max} = 1300$ km/s implies $q < 1.3$. The Young, Schneider and Shectman (1981a) analysis of eclipses of material at different velocities in the emission lines suggests $q = 0.8$ or 0.9, and we have used $q = 0.9$.

The eclipse of DQ Her is exceptionally wide, $\Delta\phi = 0.11$. To accomplish this, the mass ratio must be $q > 0.67$ and the inclination $i > 80°$ (if $q < 1.0$). Radial velocity work is hampered by emission from the nebular remnant of the 1934 nova outburst. Three photographic studies (Greenstein and Kraft 1959, Hutchings, Cowley and Crampton 1979 and Smak 1980) suggest $K_w = 140$ km/s. The extent of the emission line wings and the period of the 71-second oscillation (Walker 1956), interpreted as rotation of the white dwarf, then each rule out mass ratios larger than 1.1. We adopt $q = 0.75$ as suggested in the emission line eclipse study by Young and Schneider (1980). The system is so nearly edge-on that the eclipse geometry is quite insensitive to the uncertainty in q.

No radial velocity curves have as yet been published for UX UMa, its spectrum normally shows broad, shallow absorption lines. The eclipse is so narrow, $\Delta\phi = 0.053$, that a large fraction of the disk remains uneclipsed unless the mass ratio is very small. We take our ephemeris from Mandel (1965), finding $\phi_0 = -0.011$, and adopt $q = 0.6$ quite arbitrarily.

Radial velocity work on RW Tri by Smak (1979) and unpublished work by Horne and Oke suggest $K_{em} = 130$ km/s with a large anomalous phase lag (0.1 cycles) in the velocity curve. Mass ratios smaller than 0.4 are excluded if the accreting star is a white dwarf with $K_w = 130$ km/s, and mass ratios larger than 1.0 are eliminated by the emission line width $V_{max} = 1300$ km/s. We employ $q = 0.8$ for the results presented in this study.

For Lanning 10 we combine the 1980 eclipse timings reported by Horne, Lanning and Gomer (1982) with four additional timings, two in 1981 and two in 1982, to obtain the revised ephemeris

$$\mathrm{HJD} = 2{,}444{,}557.9500(6) + 0.3212426(3)\ E\ .$$

No evidence for period change is seen over the two-year baseline. For the eclipse in this study, we adopt $\Delta\phi = 0.055$ and $\phi_0 = -0.002$. The emission line velocity amplitude K_{em} = 240 km/s found by Horne, Lanning and Gomer (1980) was so large that no solution with $M_w < 1.4\ M_\odot$ and $q < 1$ is possible. For this study we have assumed $q = 1$.

The adopted geometric parameters are collected in Table 3, and the resulting eclipse geometries are illustrated by Figure 6. The view here is down the orbital angular momentum vector, so that the stars orbit in a counter-clockwise fashion, with the occulting lobe-star to the right. R_{L1} is taken as the unit of distance. Arches drawn on the accretion disk connect points of constant ingress and egress phase. Each of these ingress/egress arches, one of which is drawn in bold, outlines a region of the disk that is occulted at one particular phase. The potential for obtaining information about the two-dimensional structure of an accretion disk from one-dimensional eclipse light curves stems from the circumstance in close binaries that the ingress/egress arches intersect with each other at respectably large angles. By considering the response of this network of arches to changes in the geometric parameters, one may deduce approximately the effect of using incorrect values for the geometric parameters in reconstructing the disk surface brightness distribution. Experiments with simulated eclipse data substantially confirm the heuristic discussion presented below.

Small errors in ϕ_0 and $\Delta\phi$ produce only trivial changes in the eclipse geometry. Since ϕ_0 and $\Delta\phi$ determine which specific pair of ingress/egress arches cross at the center of the disk, errors in these parameters cause to first order a harmless translation which leaves the brightest part of the reconstructed map displaced from the center of the disk. The values of ϕ_0 and $\Delta\phi$, originally estimated from the eclipse profiles, were tweaked to register the bright central source in the reconstructed map with the center of the disk.

We are fortunate in view of the uncertainties in the mass ratio that the eclipse geometry is only weakly sensitive to q. The mass ratio controls the size of the occulting lobe-star relative to the Roche lobe occupied by the disk, but any change in q is offset by an accompanying change in the inclination which maintains the eclipse width $\Delta\phi$ (Figure 5). Thus, only second order distortions in the eclipse geometry result from errors in q. Note in Figure 6 the similarity among the eclipse geometries for HT Cas, UX Uma and Lanning 10, which have comparable eclipse widths but widely ranging mass ratios. The principal difference is in the size of the section at the back of the disk that avoids being eclipsed.

c) Maximum Entropy Eclipse Mapping

The calculation of a predicted eclipse light curve from a given accretion disk intensity distribution and eclipse geometry is a straightforward one (Equation 1). The inverse problem, however, that of deducing the intensity distribution from the observed eclipse light curve, is severely underdetermined. A multiplicity of different intensity distributions will predict eclipse light curves consistent with the observed one. These distributions are all equally consistent with the observations, yet some may be still be preferred over others. The maximum entropy criterion selects from among the set of consistent intensity maps the unique map which contains the least information (the entropy of the map being minus its information content). By minimizing the information content of the map, subject to constraints imposed by the eclipse observations, one may hope that any information which remains in the map will be reliable information that is required to be there by the observations.

The power and versatility of the maximum entropy method (MEM) have been amply demonstrated in applications to imaging problems from a wide variety of disciplines including medicine, astronomy, and criminology. Its debut in astronomy came with the pioneering work of Gull and Daniel (1978), who demonstrated the method's capabilities in the aperture synthesis mapping of radio sources. The method has been used to advantage in deconvolving blurred and noisy optical images (Bryan and Skilling 1980) and in X-ray astronomy (Willingale 1981). MEM produces a unique, strictly positive image from observational data that may pertain to the image in a direct or complicated way. Its ability to cope with problems in which the image is incompletely constrained by the available observations makes MEM particularly attractive for use in the construction of accretion disk images from eclipse profile observations.

In the accretion disk mapping problem, the data d(K) are observed eclipse flux profiles, the images I(J) are maps of the intensity of emission from the surface of the accretion disk, and the mapping between image space and data space is provided by the eclipse simulation (Equation 1), which associates with each image a predicted eclipse profile f(K). The entropy of the image is maximized subject to a constraint on a goodness of fit statistic C, defined on data space, which ensures consistency with the data. The simplest form for the consistency statistic, and the one employed in this work, is chi-squared

$$C = \sum_{K} \left[\frac{d(K) - f(K)}{\sigma(K)} \right]^2 \qquad (2)$$

where $\sigma(K)$ are the estimated errors in the observed fluxes d(K).

The development at Cambridge of a robust and efficient algorithm for solving numerically the constrained maximization of entropy in a high-dimensional image space is lucidly narrated in the review paper by Skilling (1981). The recommended algorithm is iterative, and operates during each iteration within a subspace spanned by ΔS and ΔC (the image space gradients of the entropy and of the consistency statistic) and by several related vectors obtained by operating on the gradients with the Hessian (second derivative) matrices $\Delta\Delta S$ and $\Delta\Delta C$. Quadratic models for C and S are used to estimate a correction to the image that will maximize $Q = \alpha S + C$ within the subspace. The Lagrange multiplier α is automatically adjusted during the iteration in order to bring the value of the consistency statistic C into agreement with its desired value.

The specific form of entropy used is

$$S = - \sum_J \frac{I(J)}{D(J)} \left[\ln\left(\frac{I(J)}{D(J)}\right) - 1 \right] \tag{3}$$

The entropy does not measure the "smoothness" of an image in the usual sense of continuity. In the definition of entropy, no use at all is made of the relative distances between various image elements. One can scramble a relatively smooth intensity map by randomly interchanging the locations of its image elements to produce a noisy map which will have exactly the same entropy as the original one. The entropy measures instead (minus) the information content of the map I(J) relative to a default map D(J).

The use of a default map D(J) in the definition of the entropy lends a useful flexibility to the method. The global (unconstrained) maximum of the entropy occurs when the intensity map and default map are identical. Thus if the default map itself is consistent with the observations, it will be the map with maximum entropy. Parts of the image that are not constrained by the observations will assume values taken from the default map. One may examine various hypotheses about accretion disks by making an appropriate choice for the default map. For example, to determine whether a particular accretion disk model is consistent with the observed light curves, it would be appropriate to use the intensity map predicted by that model as the default map.

The MEM iteration may begin with a uniform intensity map or with any simple disk model that roughly fits the eclipse data. Tests with real and simulated data show that the final results are insensitive to the initial map chosen. The eclipse geometry is held fixed while the disk intensity distribution is adjusted. Thus the occultation kernel O(J,K) needs to be calculated just once using the adopted values of ϕ_0, $\Delta\phi$, and q. The initially poor fit improves steadily during the first stage of the MEM iteration. The consistency statistic C decreases monotonically, roughly as the number of iterations to the power -4, until an acceptable value of C is achieved. Subsequent iterations serve to further increase the entropy while holding C fixed. The iteration is halted when the value of

$$\mathrm{TEST} = \frac{1}{2}\left|\frac{\Delta C}{|\Delta C|} - \frac{\Delta S}{|\Delta S|}\right| \tag{4}$$

becomes small. TEST measures the sine of the angle between the image-space vectors ΔC and ΔS, and should vanish when the constrained maximization of the entropy is correctly attained. Values of TEST as small a 10^{-4} are obtained without much difficulty in this problem.

Realistic estimates of the observational errors are needed for the maximum entropy analysis, since these determine the relative weights given to different parts of the observed eclipse profile. Flickering errors overshadow those due to photon counting statistics except near mid-eclipse. For RW Tri and LX Ser, the flickering errors in the mean eclipse profiles were estimated directly by dividing the RMS profile (Figure 3) by the square root of the number of eclipse runs that were averaged in forming the mean eclipse profile. For the other systems, the errors estimated by photon counting statistics were augmented by an ad-hoc flickering term assumed, in accord with the results of Section IId, to scale linearly with the mean intensity profile.

In the eclipse profiles for RW Tri (Figure 2), the flux level observed after the eclipse is significantly larger than that seen before the eclipse, particularly so in the U bandpass. This behavior occurs on each individual eclipse run as well as in the mean profile, and presumably reflects a systematic variation in the brightness of RW Tri with orbital phase. Systematic orbital brightness variations are commonly observed in cataclysmic binaries, although the brightness typically peaks before the eclipse near phase 0.7-0.8 and has therefore been attributed to the changing aspect of the bright spot or to its obscuration by the disk. Absorption by circumbinary material might also produce a phase-dependent brightness variation. The flat disk model employed here does not encompass such aspect variations, nor can they easily be incorporated without additional model-dependent assumptions. The orbital modulation was therefore artificially removed by dividing each eclipse profile by a linear fit to fluxes observed before and after the eclipse and multiplying by the value of the fit at mid-eclipse.

Application of MEM to the mean eclipse profiles for the B band results in the accretion disk intensity maps which appear in Figure 7. These MEM reconstructions employed a conventional definition of the entropy, i.e. equation (3) with a uniform default map set at the level of the mean intensity. The intensity was forced to vanish beyond radius 0.85 -- just outside the Roche lobe -- and on the section at the back of the disk, if any, that was not eclipsed. Most of the maps show a broad, but irregular distribution of intensity that peaks near the center of the disk. The map of the HT Cas disk shows a compact source, as expected, but narrow ridges and troughs in the intensity distribution cut across the map. The map of the disk in DQ Her is particularly pathological, showing a broad stripe of intensity running diagonally across the center of the disk.

Perhaps surprisingly, the eclipse profiles predicted by these maps achieve an excellent fit to the observations, as is shown by Figure 8. The intensity maps found by standard MEM are indeed consistent with the observations. They are, however, highly unsatisfying due to the preponderance of features which seem physically implausible. An understanding of these distortions will lead in the next subsection to a modification of the MEM procedure which produces better results.

d) Distortions in MEM Eclipse Maps

Several distinct types of distortion may be identified in the MEM accretion disk reconstructions. The most prominent of these are disturbances which track curved arcs across the intensity distribution of the disk. Their origin may be most readily understood by considering the reconstructed map of the HT Cas disk, which is dominated by a compact source at its center. Here the disturbance is concentrated along a pair of arches that intersect at the position of the compact bright source. A comparison of Figures 6 and 7 reveals that these arches correspond to the phases of white dwarf ingress and egress. The intensity is enhanced along the inner branches of each arch, where ingress or egress occur simultaneously with the white dwarf, and is depressed along the outer branches where ingress occurs as the white dwarf emerges from eclipse or vice-versa.

The information content of the HT Cas disk map is dominated by the high-intensity pixels near the center of the disk. The entropy of the map is thus favorably increased when these peak intensities are reduced. This same effect has been discussed by Bryan and Skilling (1980) in the context of MEM deconvolution of an optical photograph of the jet and nuclear region of M 87. Their MEM image was systematically low relative to the data in the vicinity of peaks. The increase in chi-squared produced by negative residuals near the peaks was offset by reduced contributions to chi-squared from other parts of the map, which followed noise in the data more closely than they should have. Bryan and Skilling partially overcame the problem by use of a more stringent consistency statistic, which forced the distribution of residuals to agree with the expected gaussian form. There is every reason to expect that biasing can be eliminated entirely in maximum entropy deconvolution problems by the use of a sufficiently powerful consistency statistic. This solution, however, does not affect the tendency of MEM to relax peaks in the accretion disk maps, since the relaxation is permitted to occur by the intrinsic weakness of the eclipse constraints rather than by noise in the data.

Let us now examine the eclipse constraints in more detail. The slope of the eclipse profile is given by a sum of positive contributions from parts of the disk that are emerging from eclipse and negative contributions from parts that are entering eclipse. Thus the observed eclipse profile effectively constrains weighted integrals of the intensity along each ingress/egress arch, with positive weights on the egress branch and negative weights on the ingress branch of the arch. The striking distortion in the HT Cas map has developed in order to preserve these line integrals, and hence the predicted eclipse profile, as the intensity of the bright central source is reduced to increase the entropy. Further discussion of the mechanics of "twin-arch" distortions, including an illuminating analytic analysis of a simpler but closely related problem from tomography, is contained in the Appendix.

Twin-arch distortions exert a serious but less pronounced influence on the other MEM accretion disk maps in Figure 7. The disk maps for LX Ser, UX Uma, RW Tri and Lanning 10 each show ridges of enhanced intensity along the ingress/egress arches that cross through the broad peak of their intensity distribution. Most of the anomalous structure seen in the MEM maps is accounted for by twin-arch distortion, which stems from inherent limitations in the constraints placed on the map by the observed eclipse profile, and are not the result of noise in the observations.

Noise in the observed eclipse profile also produces disturbances in the MEM disk map. A small flicker causing a momentary change in the slope of the eclipse profile produces a "ripple" in the intensity along the ingress/egress arch at the corresponding phase. As smaller values of chi-squared are aimed for in the MEM reconstruction, the number of such ripples rapidly increases giving the MEM map a striated appearance. This behavior has proven to be helpful in guiding the selection of an appropriate value for chi-squared when the flickering error estimates are uncertain. A pair of flickers can, of course, mimic a spurious bright spot on the disk. The only satisfactory remedy for flickering is to average together many eclipse runs in forming the mean eclipse profile.

Another distortion, which may be noted in Figure 7's maps for UX UMa and Lanning 10, is a buildup of intensity along the limit of the occultation zone. A uniform string of flux so placed along the occultation limit has the effect of adding a constant to the predicted eclipse profile while hardly altering the shape of the eclipse. Several sources, notably the red dwarf companion star, field stars contaminating the observing aperture, and that section of disk behind the occultation limit, contribute background light to the observed eclipse profile that has been omitted in the eclipse model (Equation 1). The MEM algorithm has accounted for this background light by enhancing the intensity along the occultation limit.

e) Maximally Symmetric Eclipse Maps

The distortions arising from the inherent limitations in the eclipse constraints seriously compromise the MEM reconstructions. They appear to be a fundamental limitation of the eclipse mapping technique. A partial remedy has been found which gives good results for disks that do not depart too strongly from azimuthal symmetry. The key change in procedure is to replace the default map, D(J) in the definition of the entropy by the azimuthal average of the intensity map. Since material in the accretion disk is presumably orbiting around the central object, there is at least some physical basis for expecting azimuthal symmetry, especially near the center of the disk where tidal distortions are small and orbit times as short as 10 to 20 seconds occur. Defining the information content of the map relative to its azimuthal average is tantamount to asking whether an azimuthally symmetric map exists which is consistent with the data. The map retains complete freedom to adjust its radial profile, and may in fact depart from azimuthal symmetry if that is required by the data.

Unfortunately, the uniqueness of MEM maps is lost with the modified algorithm. Noisy eclipse light curves in effect supply only upper limits to the intensity in some parts of the disk. The radial profile in these low-intensity regions, being free to vary without significantly affecting the entropy or the predicted light curve, will depend on the detailed history of the MEM iteration. The inner regions of the disk, where the intensity is large, are strongly constrained by the eclipse data and should be reliably mapped if large deviations from azimuthal symmetry do not occur there. Symmetric intensity distributions have been satisfactorily reconstructed in tests with simulated eclipse data.

In addition, an additive constant is introduced in Equation 1 to account for sources of background light. The background fluxes were set in order to suppress the formation of anomalous intensities near the occultation limit, and are only crudely determined by the data. In many cases, background levels consistent with the estimated flux from parts of the disk that are not eclipsed gave satisfactory results. Additional background flux was required for Lanning 10, UX UMa, DQ Her, and for the red channel in the eclipse of HT Cas. The red background needed for HT Cas (~0.2 milli-Janskys at R) is probably contributed by two field stars known to contaminate the observing aperture. For DQ Her, fairly secure estimates of flux contributions from the red dwarf companion star (detected by

Young and Schneider 1981), and from the nebula and a faint visual companion (both measured by Schneider and Greenstein 1979) account for about half of the flux visible at mid-eclipse. The remainder is easily accommodated by parts of the disk which are visible to each side of the red dwarf at mid-eclipse. The background flux needed for Lanning 10 is red (4 milli-Janskys at R, perhaps half that at B). About half may be due to light from the accretion disk and the remainder may plausibly be attributed to the red dwarf companion (Szkody and Crosa 1981 discuss the integrated flux distribution of Lanning 10). The background fluxes needed for UX UMa were bluer than the flux estimated from the uneclipsed back part of the disk, suggesting that we have perhaps used too large a value for the eclipse width $\Delta\phi$.

The modified MEM algorithm was used to construct the maximally symmetric accretion disk maps presented in Figure 9. Notice in the map for HT Cas how completely the twin-arch features associated with the central source are suppressed. The map now shows a very compact central source (a single bright pixel) embedded in an extended and essentially symmetric distribution of flux which can be traced out to a radius near 0.25 (in units of R_{L1}), where its surface brightness is some eight magnitudes down from that of the central pixel. The intensity profile of this extended source is determined primarily by the shape of the lower half of the HT Cas eclipse light curve, since flickering noise is greatly diminished when the compact source is eclipsed. The remaining disk maps each show a broader intensity distribution whose brighter parts are also essentially symmetric about the center of the disk. The use of an azimuthally-averaged default map in the definition of entropy, by causing flux in the MEM map to be distributed in azimuth as uniformly as the observations will tolerate, appears to considerably reduce distortion in the inner parts of the MEM accretion disk maps.

At larger radii, all of the maps show asymmetric structure associated with a bright spot located in the quadrant of the disk that is both closest to the eclipsing star and eclipsed last. The bright spots seen in the MEM accretion disk maps are considerably, and probably artificially, elongated in azimuth. In most cases a complete ring of enhanced intensity forms at the radius of the bright spot (not easily seen in the contour diagrams but visible in analog displays of the images). Twin-arch distortion interacts with the symmetrizing entropy to redistribute the bright spot flux in complex ways. For example, the flux from a single compact bright spot located at (0.6,0.15) in the UX UMa map is apparently redistributed along its ingress arch to produce a spurious bright spot at (-0.1,-0.6) and a bulge near (0.15,-0.15). The asymmetric structure in the outer parts of the MEM disk maps thus remains considerably distorted.

The radial profile of the bright spot should not be badly distorted since the egress arch running through the bright spot runs roughly parallel to lines of constant radius. The radial position of the bright spot in the MEM map is determined by the phase of the last steep rise on the egress branch of the eclipse profile, and its width is set by the rapidity of that rise. Spot radii near 0.5 to 0.6 and widths of order 0.1 to 0.2 are indicated for LX Ser, UX UMa, and RW Tri. In HT Cas and Lanning 10, larger radii near 0.8 place the bright spots very close to the critical Roche surface, but these may be spurious due to flickering.

The map of the disk in DQ Her still seems to be pathological. The disk appears to be highly asymmetric, with an extended bright spot region whose surface brightness rivals that of the central object. The surface brightness falls very slowly with radius from the center. We caution that the flat disk approximation may fail for DQ Her, whose disk is seen nearly edge-on. Obscuration of the central parts of the disk would affect the reconstructed intensity distribution.

To summarize, the MEM method can be used to find a unique, model-independent representation of the surface brightness distribution on the face of an accretion disk from observations of the eclipse of the disk by its companion lobe-star. Satisfying fits are achieved despite asymmetry in the observed eclipse light curves. The MEM disk maps are badly disfigured if the standard form of entropy is used, a result of the inadequate nature of the constraints placed on the map by the eclipse observations. The distortion can be substantially reduced in the bright central parts of the map by defining the entropy with respect to the azimuthal average of the map. The outer regions of the map remain distorted if asymmetric structure, such as a bright spot associated with the gas stream, is present. The eclipse mapping technique, while not perfect, provides useful information about the inner parts of the accretion disk, and MEM disk maps derived in this section will serve as the basis for quantitative investigation of the structure of disks, both local and global, in the forthcoming section.

IV. THE LOCAL AND GLOBAL STRUCTURE OF ACCRETION DISKS

Current theoretical models of accretion disks assume that the disks are azimuthally symmetric and physically thin. A consequence of these two assumptions is that the Keplerian orbital motion of the disk material about the central object is highly supersonic and that the pitch angle at which the material spirals inward is tiny. Some process must operate to remove angular momentum from the material in the disk in order for the material to accrete. Time-dependent accretion disk studies (Lynden-Bell and Pringle 1974) show that friction in the disk causes angular momentum to pass outward, along with a small amount of material, to larger radii while the bulk of the material in the disk moves inward. Most of the angular momentum ultimately passes back into the binary orbit through tidal interaction between the outer annuli of the disk and the companion star (Papaloizou and Pringle 1977).

The viscosity mechanism operating in disks has not yet been identified. The timescales of dwarf nova outbursts, interpreted as accretion events, suggest that the viscosity mechanism is highly efficient (Bath and Pringle 1980). If viscosity is produced by turbulence, nearly sonic eddies spanning a good fraction of the disk thickness are required. If magnetic stresses dominate, the field strengths involved must approach the buoyancy limit. Want of an adequate theoretical formulation forces a highly simplistic treatment of viscosity in accretion disk models. The most celebrated of these is the α-model of Shakura and Sunyaev (1973), in which the viscous stress is assumed to be constant fraction α of the pressure.

In a steady state, the rate at which viscous dissipation deposits energy in the disk is balanced by the rate of energy loss through radiation from its surfaces. If the mass and energy budgets balance locally, the effective temperature T_{eff} of the disk is determined independently of the viscosity, and is given as a function of radius R by the expression

$$T^4_{eff} = \frac{3GM_w\overset{o}{M}}{8\pi\sigma}R^{-3}[1-(R_0/R)^{1/2}] \ , \tag{5}$$

where $\overset{o}{M}$ is the mass transfer rate, M_w is the mass of the white dwarf at the center of the disk, R_0 is the inner radius of the disk, which might occur either at the surface of the white dwarf or at its magnetosphere, and G and σ are familiar constants.

Previous comparisons between observations and accretion disk theory have been limited to the integrated light of the disk. The standard paradigm for the interpretation of cataclysmic variable flux distributions has been a summation of blackbody spectra with temperatures distributed according to Equation 5 over the face of a symmetric disk. For $kT_{max} >> h(nu) >> kT_{min}$, the integrated spectrum assumes the familiar form $f_{(nu)} \sim (nu)^{1/3}$. At lower and higher frequencies, the integrated disk spectrum makes a gradual transition to Rayleigh-Jeans and Wien forms appropriate to the minimum and maximum temperatures of the disk. Observations both in harmony and discordance with this simple theory have been reported (Bath, Pringle and Whelan 1980, Szkody 1981). Motivation for the use of blackbody spectra is simply convenience in the absence of any secure theoretical or observational handle on what the spectrum emitted locally in an accretion disk might be. Wade (1982) has shown that disk parameters determined from integrated flux distributions change appreciably if stellar atmosphere spectra are summed rather than blackbodies.

A number of factors may play a role in shaping the spectrum that is emitted at different locations in the disk. Although the radial effective temperature profile of the steady-state disk model is independent of the viscosity mechanism, the local spectrum, depending as it does on the vertical structure of the disk, may be influenced by the viscosity. If most of the viscous dissipation occurs below the photosurface of the disk, the local spectrum might be predicted by a flux-conserving model atmosphere code and could resemble the spectrum of a stellar photosphere. Herter et al. (1979) and Mayo et al. (1980) have published integrated disk spectra for this case. If viscous dissipation occurs near the photosurface, the vertical temperature gradient could be greatly reduced causing the emergent spectrum to resemble more closely that of a blackbody. If dissipation occurs in violent localized bursts (magnetic reconnection events), the time-averaged spectrum emitted locally might be a composite of the high-temperature or non-thermal spectrum emitted during bursts and the lower-temperature ambient spectrum emitted between bursts.

Several mechanisms affecting the structure of the accretion disk have been devised to account for the emission lines that are observed in the optical and ultraviolet spectra of most cataclysmic variables. At sufficiently small mass transfer rates, temperatures become so low that hydrogen begins to recombine and the attending drop in opacity leaves the outer regions of the disk optically thin in the Paschen continuum (Williams 1980, Tylenda 1981). The reduced efficiency of radiative cooling causes the gas in the optically thin region to maintain a temperature near 7000 K in order to radiate the energy dissipated by viscosity. Hard radiation from the inner parts of the disk may be intercepted at grazing incidence heating the outer parts of the disk and producing a region of chromospheric emission (Schwarzenberg-Czerny 1981).

The eclipse mapping technique, with its capability to isolate light from different parts of the accretion disk, has an enormous potential for testing ideas about both the local emission mechanisms and the global structure of accretion disks. The spectra emitted by different parts of the accretion disk may be investigated by comparing accretion disk maps derived from observed eclipse profiles at different wavelengths. Our three-color eclipse observations, by measuring the Balmer jump and the slope of the Paschen continuum, provide enough spectral information to distinguish between the various emission mechanisms which may operate in different parts of the disk. We focus first on the local properties of disk emission and then turn to questions of global accretion disk structure.

a) Emission Mechanisms

Color-color and color-magnitude diagrams have long been standard tools for analyzing photometry of faint stars. They provide a convenient means of segregating the stars into various classes and of estimating stellar surface temperatures and gravities by comparison with stellar atmosphere models. Here the diagrams will serve as a forum for comparing the observed spectra from different parts of an accretion disk to the theoretical spectra of various emission mechanisms. Color indices determined for each pixel in the accretion disk maps for the U, B and R bandpasses are plotted in Figure 10 in the form of a color-color diagram for each accretion disk.

Since the observed colors have been derived from maximally symmetric eclipse maps, scatter in the color-color diagram reflects deviations from azimuthal symmetry rather than statistical noise and cannot be used to judge the reliability of the results. Statistical errors in the colors stemming from noise in the observed light curves and error in the absolute flux calibration do not exceed 0.1 magnitude. Distortions in the MEM maps produce systematic errors in the colors which are difficult to estimate accurately because of the complex ways in which flux may be redistributed on the disk. As the plot symbols diminishing in size with increasing radius attempt to suggest, the observed colors are most reliable for the bright inner regions of the disk.

Theoretical spectra have been convolved with the bandpass functions of Figure 1 to obtain color indices directly comparable with the observations. Optically thick thermal emission models are represented in Figure 10 by the loci of blackbodies and of main sequence stars for temperatures between 3000 K and 100,000 K. The main sequence data are taken from the Gunn and Stryker (1982) spectrophotometric stellar atlas, which is based on observations of stars with the Oke Multi-channel Spectrophotometer. The effective temperature calibration is adapted from Bohm-Vitense (1981). The track running diagonally toward the upper right represents optically thin emission by hydrogen in thermal equilibrium at temperatures from 10,000 K to 100,000 K. Power-law spectra lie along a line (not shown) passing through the origin and a point near the upper (Rayleigh-Jeans) end of the blackbody line.

The observed colors in the innermost regions of all of the disks, agree with those of optically thick thermal emission models. They fall generally into the region between the blackbody and main sequence curves at temperatures above 10,000 K. In the disk of HT Cas, the colors progress with radius toward the upper right-hand corner of the color-color diagram, indicating that the accretion disk is optically thin. A similar trend in this direction occurs at larger radii in the disks of LX Ser, DQ Her and RW Tri.

Color-magnitude diagrams for the six accretion disks may be examined in Figure 11. These are analogous to cluster color-magnitude diagrams except that here each point represents the light from a different part of the accretion disk. The B surface brightness of individual pixels, expressed on a magnitude scale, is plotted against the observed color indices B-R and U-B. The plot symbols encode the radius of the pixel in the same way as in Figure 10. In all systems except HT Cas, the B-R color index becomes redder as the B surface brightness decreases. Spurious statistical correlations might arise here, since any statistical fluctuation in B necessarily induces a like fluctuation in B-R and an opposite fluctuation in U-B, but the slope of the observed relation is far in excess of any that can be produced by such statistical effects.

The blackbody (dotted) and main sequence (solid) curves that are plotted in the color-magnitude diagrams of Figure 11 have been shifted vertically into rough alignment with the data from the inner regions of the disk, thereby setting the angular scale of each system. Normalization of the main sequence data is based on the Barnes-Evans relation between the visual surface brightness of stars with measured angular diameters and their V-R color indices (Barnes, Evans, and Moffett 1978). The slope of the observed relation between B and B-R agrees quite well with the slopes of the thermal models, reinforcing the conclusion drawn from the color-color diagrams that the inner regions of these disks are optically thick thermal radiators.

b) Distance Estimates

The identification of light from the bright inner regions of the accretion disk as thermal radiation leads to a method of measuring distances to the eclipsing cataclysmic binaries. The intensity maps are derived under the assumption that the parameter $\theta^2 = (R_{L1}/D)^2\cos(i)$ has the value 1 $(R_{\theta}/\mathrm{Kpc})^2$. The vertical shift used to register the theoretical and observed color-magnitude curves therefore effectively measures the value of θ for each system. θ is a measure of the angular scale of the system. The distance is then given in terms of observable quantities by

$$D = \frac{PK_W}{2\pi\Theta} f(q,\Delta\phi) \tag{6}$$

where the function f is plotted against the mass ratio q in Figure 12 for several values of $\Delta\phi$. Table 4 includes the values of Θ obtained from the color-magnitude diagrams and the corresponding distance estimates for assumed values of K_W and q.

The distance estimates are based on the local emission properties of the disk material and are thus independent of assumptions about the global structure of the accretion disk. We note that our 360 pc distance to DQ Her agrees substantially with the expansion parallax of its nebular shell (420±100 pc, Ferland 1980) and with a distance estimate based on the near infrared detection of the red dwarf star (400±100 pc, Young and Schneider 1981). Distances estimated with the B vs B-R relations for blackbody and stellar photosphere models differ by some 50 percent, but the U-B data indicate that the truth lies intermediate between these two cases. Thus for a given eclipse geometry, the formal uncertainty in the value of Θ is of order 20 percent.

Errors in the distance estimates are dominated by current uncertainty in the dynamical parameters of the binaries. K_W and q are poorly known for most of the stars in our sample. The distance estimates scale only linearly with K_W and depend on q both through the function $f(q,\Delta\phi)$

(Figure 12) and through θ, whose value is weakly sensitive to the assumed eclipse geometry. Future spectroscopic work to improve the dynamical parameter determinations will simultaneously improve our distance estimates. If the inner parts of accretion disks are thermal radiators, as our results suggest, this method may ultimately be a most secure means of determining distances to eclipsing cataclysmic binaries.

c) Radial Structure

Figure 13 shows the observed surface brightness and color indices plotted as functions of radius in each of the six accretion disks. These profiles are affected by distortions in the MEM maps from which they were constructed, an example of this being the spurious intensity bump near radius 0.25 in the profile for UX UMa. The structure also becomes progressively more sensitive with radius to flickering errors in the mean eclipse profile. In particular, the structure shown at large radii for HT Cas ($R > 0.25$), DQ Her ($R > 0.4$) and Lanning 10 ($R > 0.3$) is probably dominated by flickering. The vertical spread in the data, which reflects the departure from azimuthal symmetry, generally increases with radius and becomes as large as one to three magnitudes in the bright spot regions of LX Ser, UX UMa and RW Tri. Since azimuthal symmetry was maximized in forming the disk maps, the true intensity contrast in the bright spot regions is even larger than the observed spread.

Clear evidence is seen for a radial temperature gradient in the disks of nova DQ Her and the four nova-like systems. The color indices become redder as the intensity falls with radius. The observed radial intensity and color index profiles are compared in Figure 13 to the predictions of a model in which the temperature in the accretion disk varies with radius according to

$$T^4(R) = T^4(0.3)\left[\frac{0.3}{R}\right]^{\beta}[1-(R_0/R)^{1/2}] \quad . \tag{7}$$

Here, the radial power law exponent β and the temperature at radius 0.3 serve as parameters. Both blackbody and main-sequence disk models are shown by the curves in Figure 13. The parameter values obtained in these fits are collected in Table 5. Values of R_0 near 0.015 were needed to suppress a steep rise in the predicted intensity at small radii that was not observed. The expected radius of a white dwarf is comparable to this value, as is the pixel size used in the reconstructed disk maps.

The observed radial structure permits a sensitive and unprecedented test of the standard steady-state viscous accretion disk model. In the standard model, the parameter β has the value 3, reflecting the rate at which viscous heating falls with radius in a Keplerian disk. The observed values of β, as listed in Table 5, range from 1 for DQ Her to 2.7 for UX UMa, indicating that the radial temperature gradients are not so steep as those predicted by the standard viscous accretion disk model. The fitted values of β are uncertain by perhaps 0.5 if the values for Θ are reliable. In simulations with eclipse profiles comparable in SNR and in degree of asymmetry to those observed, the radial temperature gradients were recovered to this accuracy. This result may be seen more directly in Figure 14, which shows a brightness temperature based on the B intensity plotted against disk radius on a log-log scale. A diagonal line indicates the slope of the temperature-radius relation predicted by the standard model. The observed temperature gradients are all smaller than the standard disk model prediction.

The temperature at each radius in the disk is determined in the standard model by a balance between viscous heating and radiative cooling. The radial temperature gradient of the model may be reduced by processes that heat the disk material preferentially at large radii or that cool it at small radii.

Acoustic or MHD waves are unlikely to propagate far in the radial direction across the strong sheer in the disk. They could transport energy vertically, however, heating a corona above and below the plane of the disk and cooling material at the optical photosurface. Observed time delays between correlated x-ray and optical flares (x-ray following optical) suggest that this process occurs in the disk of TT Ari (Jensen et al., 1982). Backwarming would limit the rate of cooling at the photosurface to of order half the local viscous dissipation rate, a rate not sufficient to produce the observed effect.

Mass lost in a wind from the inner parts of the disk could remove energy from the disk preferentially at small radii. Winds are evidenced in low-inclination cataclysmic binaries by the P-Cygni line profiles of ultraviolet emission lines (Greenstein and Oke 1982, Cordova and Mason 1982). The observed wind velocity is of order the escape velocity from a white dwarf, but the estimated mass loss rates are only of order a percent of the mass transfer rate, and so the wind cannot significantly cool the inner regions of the disk.

The most viable means of reducing the radial temperature gradient is through irradiation of the face of the disk by hard photons from the center of the disk. This mechanism has been advocated by Schwarzenberg-Czerny (1981) to account for discrepancies between the observed UBV colors of cataclysmic variables and colors calculated for the integrated emission from viscous accretion disk models. The kinetic energy of material orbiting at the inner radius of the disk is dissipated in a boundary layer where the material accretes onto the surface of the white dwarf (Pringle 1977). If the white dwarf does not rotate too rapidly, the bolometric luminosity of the boundary layer will rival that of the entire disk. A modest fraction of the x-ray or EUV luminosity emitted by the boundary layer will be intercepted by the disk. The irradiative heating rate per unit area will fall off somewhat more slowly than R^{-2} on the concave face of the accretion disk. Since viscous heating drops out as R^{-3}, the energy budget must be dominated by irradiation at sufficiently large radii. Further support for this explanation of the observed temperature gradients is provided by an apparent correlation between the observed radial temperature gradient and the prominence of emission lines in the optical spectrum. DQ Her and LX Ser, the systems in our study with the smallest radial gradients, show strong line emission while UX UMa, whose radial gradient is nearly consistent with viscous dissipation alone, shows an absorption line spectrum. Both line emission and diminished radial temperature gradients are likely consequences of irradiative heating.

On the assumption that viscous heating in the disk is augmented by some additional heating processes and that cooling is by thermal radiation alone, an upper limit to the mass transfer rate may be found by setting $\beta = 3$ in Equation 7 and locating the largest value for T(0.3) that predicts disk intensities which remain below those observed at all radii. The mass transfer rate is then given by

$$\mathring{M} = (1.7\text{X}10^{-10}\ \frac{M_\odot}{yr})\left[\frac{P}{hr}\right]^2\left[\frac{T(0.3)}{10000K}\right]^4 g(q) \ ,$$

(8)

where the function $g(q)$ varies from 1.0 at $q = 1$ to 1.25 at $q = 0.3$ and is effectively ignorable in view of the uncertainty in $T^4(0.3)$. The mass transfer rate upper limits so obtained are listed in Table 5. These limits take into account the inclination, but neglect limb darkening and interstellar reddening. The upper limits found here are smaller by factors of 10 to 100 than the 10^{-8} $M_\odot$/yr rate thought to be typical of classical novae and nova-like variables. The neglect of optical reprocessing of hard radiation may well have caused systematic overestimation of mass transfer rates in previous work. The lower transfer rates found here are in better agreement with the rates predicted by gravitational radiation than were previous estimates.

d) The Naked Boundary Layer in HT Cas

The compact bright source in the center of the disk in HT Cas is contained substantially within a single pixel of the MEM accretion disk map, adjacent pixels being some 2 magnitudes fainter. The central pixel is located in the color-color diagram near the blackbody line around a temperature of 12,000 K. If the compact source is indeed the photosphere of the white dwarf, the vertical shift in the color-magnitude diagram leads by the methods of Section

IVb to $\theta \sim 3.3$ and a distance $D \sim 70$ pc. This distance becomes even smaller if the white dwarf fails to completely fill the central pixel. This distance limit seems unreasonably small, since the absolute visual magnitude of the system would then be larger than 12.

Three additional considerations argue against the interpretation of the central source as the white dwarf photosphere. First, a DA white dwarf at this temperature has broad Balmer absorption lines which would appear in the optical spectrum as broad absorption wings on either side of the emission line profile from the disk. Such wings are not observed (Young and Schneider 1981). The white dwarf is certainly of DA type, since it continually accretes hydrogen-rich material from the disk. The absorption lines cannot simply be filled in by the disk's emission lines since the former would still become evident during certain stages of the eclipse. Second, the central source in HT Cas flickers with amplitudes of 10 - 30 percent and rise times as short as 30 seconds. The cooling timescale for a white dwarf is vastly longer than this. Finally, from the color-magnitude diagram for HT Cas, the colors of the light emitted by the material immediately surrounding the central source are those of optically thick thermal emission at temperatures of 15,000 K to 20,000 K (Figure 10). However, the surface brightness in these regions is smaller by several magnitudes than that of the central pixel (Figure 11a), implying if the central source is the white dwarf photosphere that the surrounding material is optically thin.

These difficulties are avoided if the compact central source represents a composite of the white dwarf photosphere and hot optically thin gas from the boundary layer. The 12,000 K blackbody colors and 70 pc distance found above are then spurious. Flickering will arise as fluctuations in the rate at which gas from the disk arrives at the surface of the white dwarf modulate the hot free-free component from the boundary layer. The gas in the surrounding accretion disk is optically thin, perhaps becoming marginally optically thick as it approaches the center of the disk. The corresponding boundary layers in the other systems may be obscured by the surrounding optically thick accretion disk. A detailed analysis of ionization conditions in the optically thin disk of HT Cas will be possible when photometric eclipse observations with higher spectral resolution are in hand.

V. SUMMARY AND PROSPECTUS

This paper presents an observational study of the spatial structure of the accretion disks in six cataclysmic binaries. Surface photometry of the accretion disk is made possible by exploiting the unique mapping capability provided by the eclipse of the disk by its companion lobe-star. For the first time, the emission from different parts of an accretion disk are isolated for study.

High-speed three-color eclipse photometry, obtained with the Palomar and Mt. Lemmon 60-inch telescopes, provides the observational basis for this study. Several eclipse cycles of each system were observed when possible in order to diminish the impact of flickering in the mean eclipse profiles that were formed by averaging together data from several eclipse cycles. A sufficient number of eclipses was obtained to permit a crude determination of the distribution of flickering from the disks in LX Ser and RW Tri. The flickering appears to be widely distributed on the face of these disks.

The inversion of an eclipse profile to obtain the accretion disk surface brightness distribution is nontrivial. The problem resembles that of tomographic reconstruction with only two viewing angles. A maximum entropy technique is used to accomplish the inversion. The standard MEM reconstructions of accretion disk intensity distributions achieve satisfying fits to the observed light curves, but are seriously compromised by distortions produced along lines of constant ingress and egress phase. The origin of these distortions is identified and their formation is greatly suppressed by altering the definition of the entropy so that only deviations from azimuthal symmetry are important. Reconstructions made with the modified form of entropy are maximally symmetric in azimuth, and are suitable for detailed study of the emission from the bright inner regions of the disks.

The disks of nova DQ Her and four nova-like systems all show a broad intensity distribution which extends to large radii at which the disks would be limited by tidal interaction with the companion star. In contrast, the disk of the quiescent dwarf nova HT Cas is smaller and is dominated by a compact source at its center. Bright spots presumably associated with the gas streams which feed the disks are evident, but their spatial structure is not accurately reconstructed by the present mapping technique.

The spectral character of light from different parts of the accretion disks is investigated by means of color-color and color-magnitude diagrams. The bright inner parts of the disks in the nova and nova-like systems are found to lie between blackbody and main sequence loci in the color-color diagram, suggesting that these regions are optically thick thermal radiators. The suggestion is confirmed by the color-magnitude diagrams which show relations between the surface brightness and color indices that are consistent with thermal radiation. The identification of the disk emission as thermal fixes the angular scale of each disk and leads to a determination of distances by a method analogous to cluster main sequence fitting. The distance estimates are independent of the global structure of the disks, but depend on dynamical parameters of the binaries which are currently uncertain.

Radial temperature gradients in the nova and nova-like disks are generally not so steep as the $R^{-3/4}$ law predicted by steady-state viscous accretion disk theory. The most plausible explanation for this result is that irradiation dominates viscous dissipation as a heating source in the outer parts of the disks so that much of the optical radiation from the disk is reprocessed light. Upper limits to the mass transfer rates based on this interpretation are smaller by one or two orders of magnitude than previous and widely accepted estimates for novae, and are in better agreement with rates predicted by gravitational radiation. Mass transfer rates for novae and nova-like variables may have been systematically overestimated in the past due to the neglect of reprocessed light.

The extended accretion disk in HT Cas is optically thin. The bright compact source at its center is very likely a composite of photospheric radiation from the white dwarf and free-free emission of variable intensity from hot gas in the accretion boundary layer.

The eclipse mapping technique is an important new tool which should lead to further advances in our understanding of the accretion disks in close binary systems. The temperature structure of the disks and the question of optically thin material in the outer regions can be much more sensitively investigated by application of the eclipse mapping technique to simultaneous infrared and optical eclipse photometry. Extension to the ultraviolet will also be useful in following the temperature gradient to smaller radii and in firmly establishing the geometric eclipse parameters, but this must await the arrival of the Space Telescope. Eclipse profiles for Balmer, He I and HeII line emission can be used to construct maps of the emission line regions. The spatial relations between the emission regions for lines of different excitation should lead to an unambiguous identification of the excitation mechanisms responsible for the line emission. Finally there is the possibility of studying in some detail the spatial distribution of flickering activity by acquiring photometry for a large sample of eclipses and constructing a map from the RMS eclipse profile. If flickering is widely distributed throughout the disk, as is indicated by our crude result for RW Tri and LX Ser, then it may be intimately associated with the viscosity mechanism.

APPENDIX

IMAGE ARTIFACTS IN TOMOGRAPHY

Prominent artifacts distort the accretion disk intensity map that is reconstructed by the maximum entropy method (MEM) from an observed eclipse profile. The artifacts develop principally along a pair of crossed arches, loci of constant ingress or egress phase, which intersect at the position of any compact bright source on the map. The artifacts result from the inherent conservatism of MEM estimation combined with the nature of the constraints placed on the map by the observed eclipse curves.

The observed eclipse profile alone does not contain sufficient information to uniquely specify the accretion disk intensity distribution. The slope of the eclipse profile is given by a sum of negative contributions from parts of the disk that are being occulted and positive contributions from parts of the disk that are emerging from eclipse. The slope at any particular phase may thus be expressed as a weighted integral of the intensity along the ingress/egress curve which bounds the region of the disk that is occulted at that phase. Only these line integrals of the intensity are constrained by the eclipse observations.

Constraints of a similar nature are encountered in tomography, where the density on a two-dimensional slice of a three-dimensional object is reconstructed from observations of the column density along various paths through the object in the plane of the slice. In tomographic reconstructions, the number of viewing angles may usually be increased until sufficient information is obtained for a satisfactory reconstruction. The eclipse mapping problem, however, offers only two viewing aspects, those corresponding to ingress and egress. In fact, unless the the eclipse is total, somewhat less information is available in eclipse mapping than in two-angle tomography.

An analogy may be drawn between the artifacts which occur in the eclipse mapping problem and similar ones which develop along the viewing directions in tomography when the number of viewing angles is small. The simple geometry permits an analytic analysis of the tomographic artifacts which leads in turn to a better understanding of the eclipse mapping distortions.

Consider the example of an N X N intensity map in which sums of the intensity along each row and column are fixed exactly by observations. Allow the intensity to be uniform at the level B except on a single pixel, where the intensity is somewhat higher at A. A symmetric perturbation which preserves all row and column sums gives an intensity $A - (N-1)\varepsilon$ to the bright pixel, $B + \varepsilon$ to the $2(N-1)$ pixels which fill out the row and column containing that pixel, and

$B - \varepsilon/(N-1)$ to the $(N-1)^2$ pixels in the remainder of the map. The entropy of the perturbed map,

$$\begin{aligned} S = &- (N-1)^2 \, (B-\varepsilon/(N-1)) \, [\ln(B-\varepsilon/(N-1)) - 1] \\ &- 2(N-1) \, (B+\varepsilon) \, [\ln(B+\varepsilon) - 1] \\ &- (A-(N-1)\varepsilon) \, [\ln(A-(N-1)\varepsilon) - 1] \quad , \end{aligned}$$

increases with the perturbation parameter ε, since

$$\frac{dS}{d\varepsilon} = (N-1)\ln[B-\varepsilon/(N-1)] - 2(N-1)\ln[B+\varepsilon] + (N-1)\ln[A-(N-1)\varepsilon]$$

has the value $(N-1)\ln(A)$ when ε is small. The entropy is maximized when

$$\frac{\varepsilon}{B} = \frac{A - B}{(N+1)B + A/(N-1)} \; .$$

Thus the intensity of the bright pixel is considerably reduced in the MEM reconstruction, this being advantageous by increasing the maps total entropy, while the intensity on the remainder of the bright pixel's row and column is moderately enhanced and the intensity throughout the remainder of the map is slightly diminished in order to maintain the row and column sums.

The eclipse ingress and egress arches which cross at a compact bright source in an accretion disk correspond to the row and column of the intense pixel in the tomographic example. In the MEM reconstruction of the accretion disk intensity map, the intensity of the compact bright source is depressed, thereby increasing the entropy of the map, while on the remainder of the map, principally along the arches, the intensity adjusts to hold the predicted eclipse light curve into agreement with the observations. The sign of the intensity perturbation is negative along the two outer branches of the arches, since intensity there contributes to the derivative of the light curve with a sign opposite to that of the contribution from the compact source. Apart from these geometric complexities, the origin of the distortions that occur in MEM eclipse maps closely parallels that of their simpler counterparts in tomography.

TABLE 1

OBSERVATIONS OF ECLIPSING CATACLYSMIC BINARIES

Run	Star	Date 1982	UT	Sample (s)	Binary cycle	Phase range
317	LX Ser	20 June	6:01- 8:18	1.0	5351	-0.28 +0.33
320	LX Ser	21 June	4:51- 7:07	1.0	5357	-0.28 +0.33
322	UX UMa	22 June	4:10- 7:01	1.25	90514	-0.29 +0.32
324	UX UMa	23 June	4:17- 7:08	1.25	90519	-0.19 +0.43
326	LX Ser	24 June	4:54- 7:05	1.0	5376	-0.39 +0.22
329	LX Ser	26 June	4:57- 8:22	1.5	5389	-0.69 +0.22
335	Lanning 10	17 Sept	11:21-12:25	1.0	2092	-0.05 +0.08
338	RW Tri	18 Sept	8:45-11:02	1.0	70943	-0.20 +0.21
339	RW Tri	19 Sept	7:29- 9:46	1.0	70947	-0.12 +0.07
342	RW Tri	20 Sept	5:06- 7:26	1.0	70951	-0.21 +0.19
343	Lanning 10	20 Sept	7:49-10:32	1.2	2101	-0.17 +0.17
344	RW Tri	20 Sept	10:58-12:49	1.0	70952	-0.18 +0.09
345	DQ Her	21 Sept	3:32- 5:48	1.0	53087	-0.25 +0.21
347	RW Tri	21 Sept	8:57-11:13	1.0	70956	-0.23 +0.18
349	DQ Her	22 Sept	2:41- 4:57	1.0	53092	-0.26 +0.23
352	RW Tri	22 Sept	7:28- 9:45	1.0	70960	-0.18 +0.23
355	HT Cas	23 Sept	6:17- 7:25	0.5	20473	-0.48 +0.16
357	HT Cas	23 Sept	7:55- 9:29	2.0	20475	-0.43 +0.46
358	HT Cas	23 Sept	9:37-10:59	0.6	20476	-0.47 +0.30
359	HT Cas	23 Sept	11:03-12:24	0.6	20477	-0.65 +0.10

TABLE 2

BROADBAND AB79 PHOTOMETRIC SYSTEM

band	λ_{eff}	λ_{rms}	⟨ext⟩	19445	84937	+17°4708	+26°2606
U.....	3590	220	0.596	9.02	9.26	10.50	10.71
B.....	4220	380	0.280	8.35	8.55	9.75	10.01
V.....	5360	385	0.163	8.04	8.30	9.45	9.71
R.....	6530	425	0.112	7.86	8.18	9.30	9.56
I.....	7850	570	0.080	7.78	8.12	9.21	9.48

TABLE 3

ADOPTED ECLIPSE PARAMETERS

Star	ϕ_0	$\Delta\phi$	q	i	Ephemeris source
HT Cas....	-0.003	0.050	0.35	76.65	Patterson(1981)
LX Ser....	-0.017	0.081	0.9	74.89	Horne(1980)
DQ Her....	+0.005	0.110	0.75	85.27	Africano and Olson(1981)
UX UMa....	-0.011	0.053	(0.6)[1]	(73.96)	Mandel(1965)
RW Tri....	+0.005	0.078	(0.8)[1]	(75.26)	Africano et.al.(1978)
Lanning 10	-0.002	0.055	(1.0)[1]	(71.14)	this work

[1] Mass ratio is unknown, values in parentheses were chosen arbitrarily.

TABLE 4

DISTANCE ESTIMATES[1]

Star	Period (hrs)	q	K_w (km/s)	θ	Distance (pc)
HT Cas...............	1.77	0.35	115	3.3[2]	70[2]
LX Ser...............	3.80	0.9	160	0.87	460
DQ Her...............	4.65	0.75	140	0.69	360
UX UMa...............	4.72	(0.6)	(100)	1.66	(680)
RW Tri...............	5.57	(0.8)	130	1.53	(330)
Lanning 10..........	7.71	(1.0)	240	1.20	(1100)

[1] Values in parenthesis are for illustrative purposes only.

[2] Assumes compact central source is a 12,000°K blackbody.

TABLE 5

DISK STRUCTURE PARAMETERS

Star	Θ	R_0	T(0.3) (1000K)	β	$\mathring{M}$ ($10^{-10} M_\odot yr^{-1}$)
LX Ser..............	0.87	0.015	9.7	1.2	< 0.6
DQ Her..............	0.69	0.015	10.5	1.0	< 1.
UX UMa..............	1.66	0.015	9.0	2.7	< 9.
RW Tri..............	1.53	0.015	9.7	2.2	< 3.
Lanning 10..........	1.20	0.015	7.0	2.0	< 2.

REFERENCES

Africano,J.L., Nather,R.E., Patterson,J. and Robinson E.L., 1978, *Pub.A.S.P.*, **90**, 568.

Africano,J.L and Olson,E.C., 1981 *Publ.A.S.P.*, **93**, 130.

Barnes,T.G., Evans,D.S. and Moffett,T.J., 1978, *M.N.R.A.S.*, **183**, 285.

Bath,G.T. and Pringle,J.E., 1981, *M.N.R.A.S.*, **194**, 967.

Bath,G.T. and Pringle,J.E. and Whelan,J.A.J., 1980, *M.N.R.A.S.*, **190**, 185.

Bohm-Vitense,E., 1981, *Ann.Rev.Astr.Ap.*, **19**, 295.

Bryan,R.K. and Skilling,J., 1980, *M.N.R.A.S.*, **191**, 69.

Cordova,F.A., and Mason,K.O., 1982, Ap.J., **260**, 716.

Ferland,G.J., 1980, *Observatory*, **100**, 166.

Frank,J. and King,A.R., 1981, *M.N.R.A.S.*, **195**, 227.

Frank,J., King,A.R., Sherrington,M.R., Jameson,R.F. and Axon,D.J., 1981, *M.N.R.A.S.*, **195**, 505.

Greenstein,J.L. and Kraft R.P, 1959, *Ap.J.*, **130**, 99.

Gull,S.F. and Daniel,G.J., 1978, *Nature*, **272**, 686.

Gunn,J.E. and Stryker,L.L, 1982, preprint.

Herter,T., Lacasse,M.G., Wesemael,F., and Winget,D.E., 1979, *Ap.J.Suppl.*, **39**, 513.

Hildebrand,R.H. Spillar,E.J. and Stiening,R.F., 1981, *Ap.J*, **248**, 268.

Horne,K., 1980, *Ap.J.*, **242**, L167.

Horne,K. Lanning,H.H. and Gomer,R., 1982, *Ap.J.*, **252**, 681.

Hutchings,J.B., Cowley,A.P. and Crampton,D., 1979, *Ap.J.*, **233**, 500.

Jensen,K.A., Cordova,F.A., Middleditch,J., Mason,K.O., Grauer,A.D., Horne,K. and Gomer,R., 1982, preprint.

Lynden-Bell,D. and Pringle,J.E., 1974, *M.N.R.A.S.*, **168**, 603.

Mandel,O.E., 1965, *Perem.Zvesdy*, **15**, 474.

Mayo,S.K., Wickramasinghe,D.T., and Whelan,J.A.J., 1980, *M.N.R.A.S.*, **193**, 793.

Mochnacki,S.W., 1971, M.S. Thesis, University of Canterbury, New Zealand.

Nather,R.E. and Robinson,E.L., 1974, *Ap.J.*, **190**, 637.

Oke,J.B. and Gunn,J.E. 1983, *Ap.J.*, in press.

Paczynski,B. 1971, *Ann.Rev.Astr.Ap.*, **9**, 183.

Papaloizou,J. and Pringle,J.E., 1977, *M.N.R.A.S.*, **181**, 441.

Patterson,J., 1981, *Ap.J.Suppl.*, **45**, 517.

Pringle,J.E., 1977, *M.N.R.A.S.*, **178**, 195.

Schneider,D.P. and Greenstein,J.L., 1979, *Ap.J.*, **233**, 935.

Shakura,N.I. and Sunyaev,R.A., 1973, *Astr.Ap.*, **24**, 337.

Schwarzenberg-Czerney,A., 1981, *Acta Astr.*, **31**, 241.

Skilling,J., 1981, *Algorithms and Applications*, presented at Workshop on Maximum Entropy, Laramie, Wyoming.

Smak,J., 1979, *Acta Astr.*, **29**, 469.

______, 1980, *Acta Astr.*, **30**, 267.

Szkody,P., 1981, *Ap.J.*, **247**, 577.

Szkody,P., and Crosa,L. 1981, *Ap.J.*, **251**, 620.

Tylenda,R., 1981, *Acta Astr.*, **31**, 127.

Wade,R.A. 1981, Talk presented at Workshop on Cataclysmic Variables, Santa Cruz, California.

Wade,R.A. 1982, preprint.

Walker,M.F., 1965, *Ap.J.*, **123**, 68.

Warner,B. and Nather,R.E., 1971, *M.N.R.A.S.*, **152**, 219.

Webbink,R.F. 1977, *Ap.J.*, **211**, 486.

Williams,R.E., 1980, *Ap.J.*, **235**, 939.

Willingale,R., 1981, *M.N.R.A.S.*, **194**, 359.

Young,P. and Schneider,D.P., 1980, *Ap.J.*, **238**, 955.

______, 1981, *Ap.J.*, **247**, 960.

Young,P., Schneider,D.P. and Shectman,S., 1981a, *Ap.J*, **244**, 259.

———, 1981b, *Ap.J.*, **245**, 1035.

FIGURE CAPTIONS

Figure 1. Calculated response profiles for the five bandpasses available on the multi-color photometer. The data used in the present study were taken in the U, B, and R bandpasses.

Figure 2. Averaged eclipse profiles at U ( ), B ( ), and R ( ) were formed for six eclipsing cataclysmic binaries by averaging together observed light curves obtained on several eclipse cycles. The influence of random "flickering" is thereby greatly reduced. Shown also for the B bandpass only are the differences between the individual eclipse light curves and their mean. The diminution of flickering during the eclipse is clearly evident. One milli-jansky corresponds to magnitude AB = 16.4.

Figure 3. RMS eclipse profiles in the B bandpass were formed for LX Ser and RW Tri by computing at each binary phase the standard deviation of fluxes observed on 4 and 6 different eclipse cycles respectively. These curves show the eclipse of the time-variable component of the accretion disk's light.

Figure 4. Color indices U-B ( ) and B-R ( ), derived from the mean eclipse profiles of Figure 2, demonstrate the complex spectral changes that occur during the accretion disk eclipses.

Figure 5. In an eclipsing cataclysmic binary, the observed phase width $\Delta\phi$ of the eclipse by the lobe-star of the bright source at the center of the accretion disk imposes a relation, shown in this figure, between the mass ratio q and inclination of the binary. To each eclipse width there corresponds a lower limit on the mass ratio which occurs at 90° inclination.

Figure 6. The eclipse geometry adopted for each of the six eclipsing binary systems is illustrated here by a network of ingress/egress arches crossing the face of the accretion disk. Each arch, one of which is drawn in bold, is the boundary of the region of the disk that is occulted by the lobe-star at a particular binary phase. The unit of distance is that from the white dwarf at the center of the disk to the inner Lagrangian point.

Figure 7. Isophote maps for six accretion disks derived from observed eclipse profiles for the B bandpass. The maps were constructed by maximizing their total entropy, defined relative to the mean intensity, within the constraints imposed by the observed eclipse profile. Contours occur at half-magnitude intervals relative to the peak of each map. The origin of the conspicuous artifacts, which result from the incomplete nature of the information available in the eclipse profile, are discussed in section IIId of the text.

Figure 8. The fit achieved by the maximum entropy eclipse mapping method is excellent despite asymmetry in the observed eclipse profiles.

Figure 9. Isophote maps derived from the same data and with the same maximum entropy technique as that used for the maps in Figure 7, but with a modified entropy defined relative to the map's azimuthal average. These maps are maximally symmetric about the center of the disk, yet consistent with the observed eclipse data. Artifacts associated with the center of the disk are largely eliminated, while those related to the bright spot remain.

Figure 10. These color-color diagrams show the spectral character of light emitted from different parts of the accretion disk. Each point derives from a single pixel in maps like those of Figure 9 for the U, B, and R bandpasses. The plot symbols encode radius from the center of the disk, larger filled symbols being used for smaller radii. Due to distortion by flux mobility in the MEM maps, the color indices for the faint outer regions of the disk are far less reliable than those for the bright inner regions. The loci of blackbody, main sequence and optically-thin LTE hydrogen recombination spectra are shown for comparison. The innermost regions of each disk lie intermediate between the blackbody and main sequence loci.

Figure 11. The B surface brightness of individual pixels is plotted as a function of U-B and of B-R color indices. The plot symbols encode the radius as in Figure 10. These color-magnitude diagrams strongly indicate that the inner regions of the disks are optically thick thermal radiators. On this assumption, the main sequence and blackbody loci have been shifted vertically into agreement with the observations, thereby determining the angular scale parameter Θ which when combined with dynamical information leads to a distance estimate for each accretion disk.

Figure 12. The distance D to an eclipsing cataclysmic binary may be estimated from its orbital period P, white dwarf radial velocity amplitude K_W, and angular scale parameter Θ determined from the vertical shift in Figure 11. Shown here is the dependence of the distance estimate on the mass ratio q for various eclipse phase widths $\Delta\phi$.

Figure 13. The radial structure of the accretion disks is shown by the observed B surface brightness and color indices R-B+6 and B-U+8. Scatter reflects deviations from azimuthal symmetry rather than statistical noise in the results. The HT Cas disk is optically thin. In the other disks, the color indices redden (red is upward) as the intensity falls with radius. The implied radial temperature gradients are not as steep as those predicted by a steady-state viscous accretion disk model. The prediction of a fitted power-law disk model, both blackbody and

main-sequence, are shown.

Figure 14. The brightness temperature corresponding to the observed B intensity is plotted as a function of radius for nova DQ Her and four nova-like systems. The slope of the diagonal line shows the $R^{-3/4}$ law predicted by a viscous accretion disk model. The observed radial temperature gradients are all smaller than the model prediction. This effect is accounted for if most of the optical emission from the disks results from reprocessing of hard radiation emitted by the center of the disk.

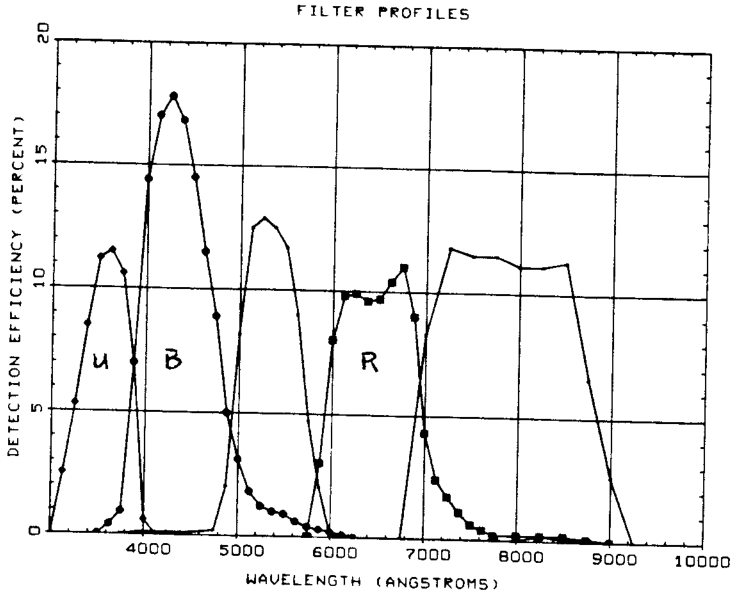
FILTER PROFILES
DETECTION EFFICIENCY (PERCENT)
0
5
10
15
20
4000
5000
6000
7000
8000
9000
10000
WAVELENGTH (ANGSTROMS)
U
B
R

Figure 1

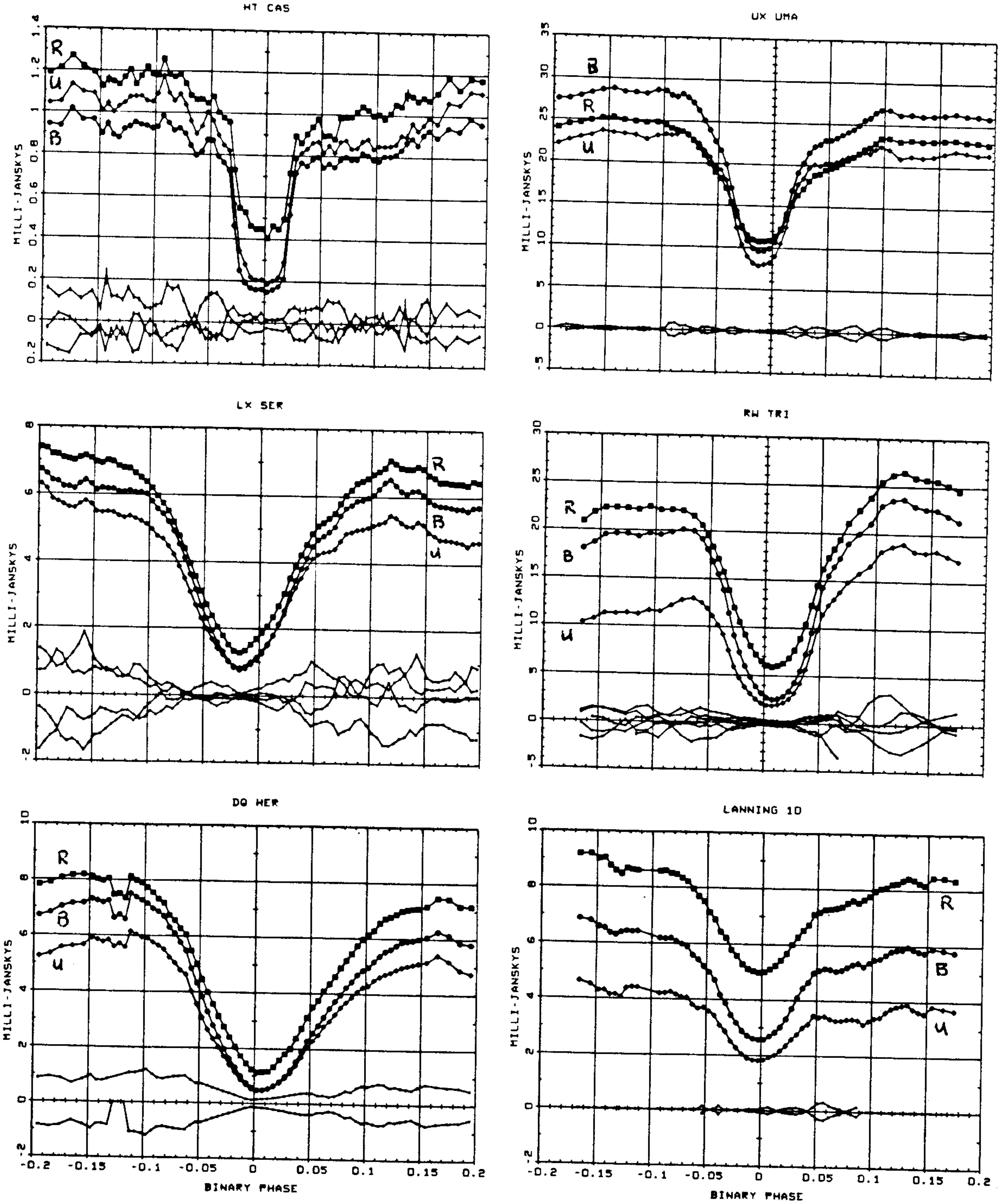
HT CAS
UX UMA
LX SER
RW TRI
DQ HER
LANNING 10
MILLI-JANSKYS
BINARY PHASE
R
U
B
-0.2
0
0.2
0.4
0.6
0.8
1
1.2
1.4
-5
0
5
10
15
20
25
30
35
-2
2
4
6
8
10
-0.15
-0.1
-0.05
0.05
0.1
0.15

Figure 2

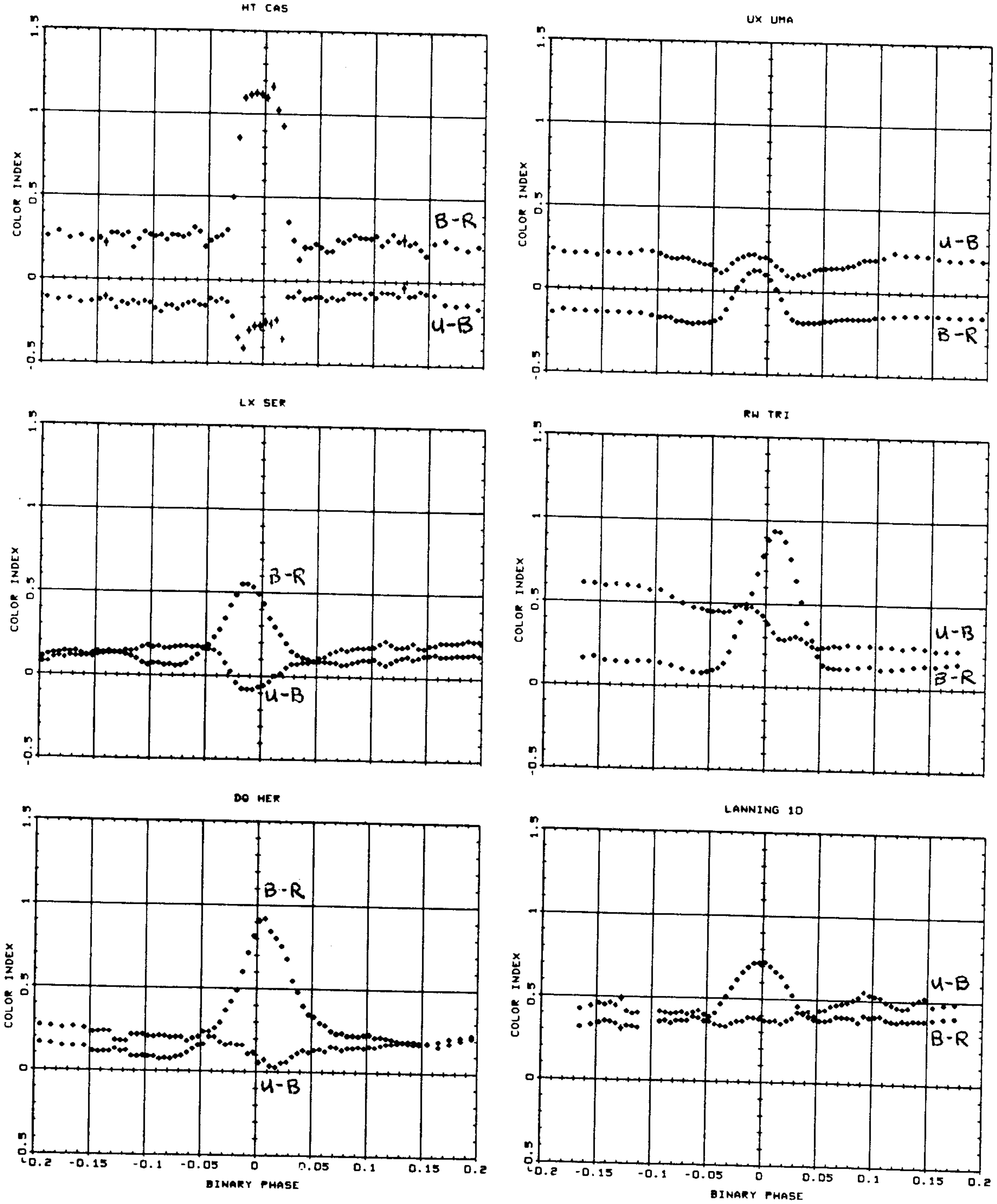
HT CAS
UX UMA
LX SER
RW TRI
DQ HER
LANNING 10
COLOR INDEX
1.5
1
0.5
0
-0.5
B-R
U-B
-0.2
-0.15
-0.1
-0.05
0
0.05
0.1
0.15
0.2
BINARY PHASE

Figure 3

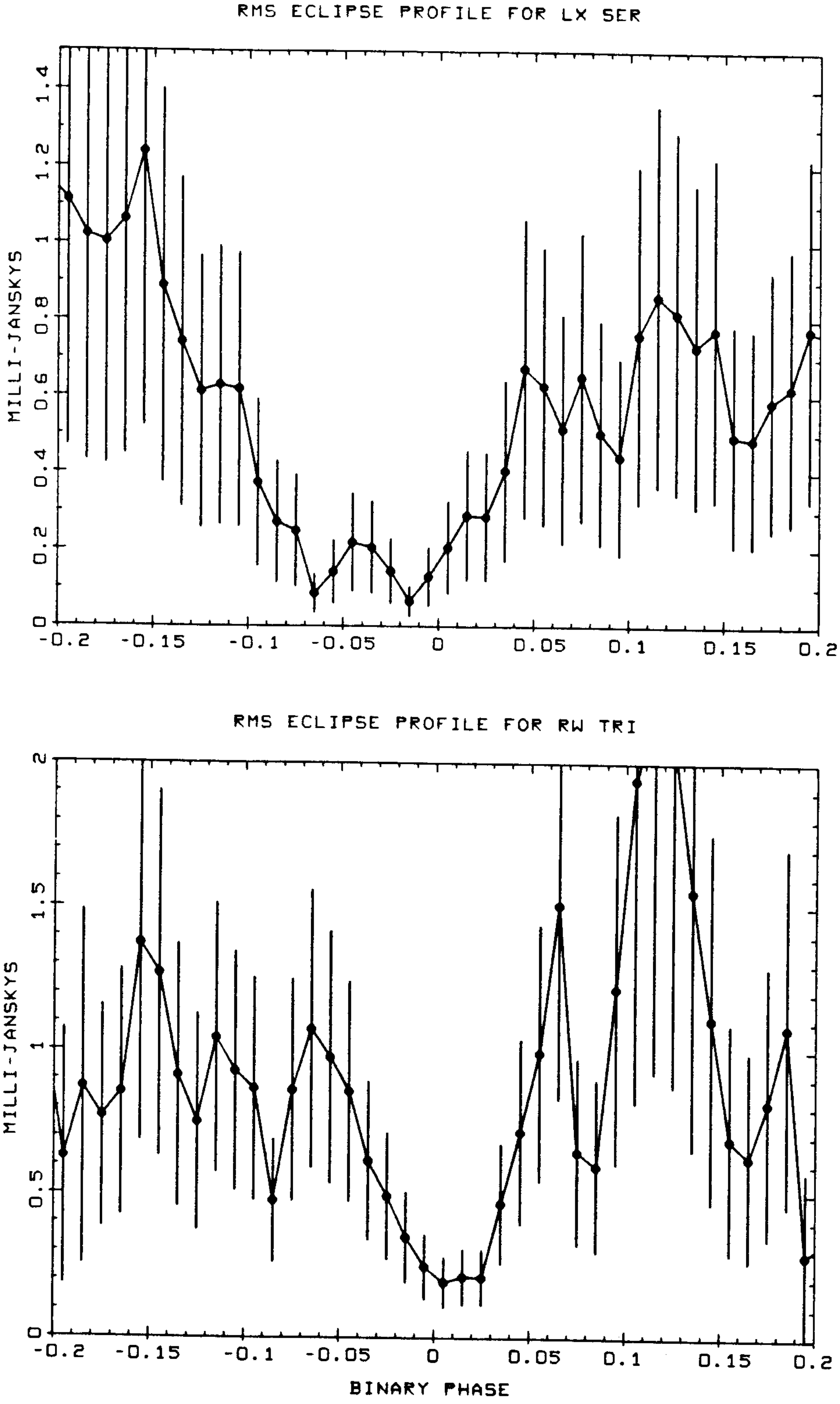
RMS ECLIPSE PROFILE FOR LX SER

RMS ECLIPSE PROFILE FOR RW TRI

Figure 4

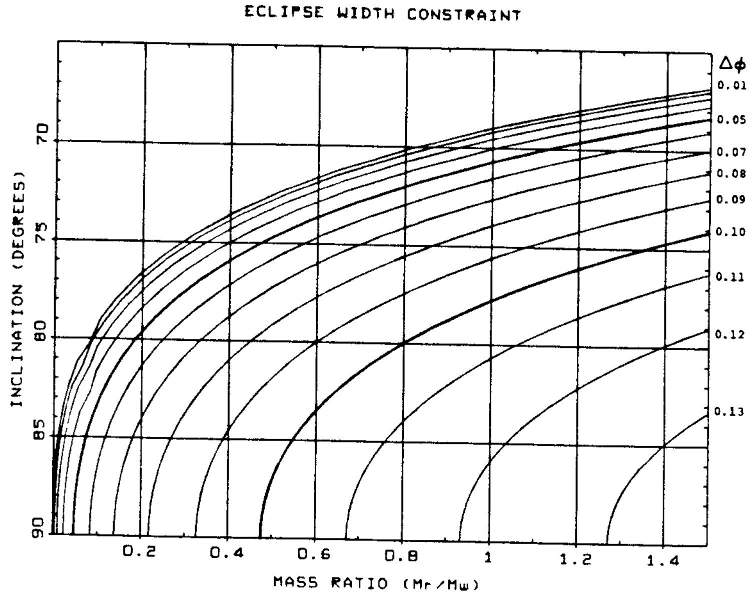
ECLIPSE WIDTH CONSTRAINT
INCLINATION (DEGREES)
70
75
80
85
90
0.2
0.4
0.6
0.8
1
1.2
1.4
MASS RATIO (Mr/Mw)
Δφ
0.01
0.05
0.07
0.08
0.09
0.10
0.11
0.12
0.13

Figure 5

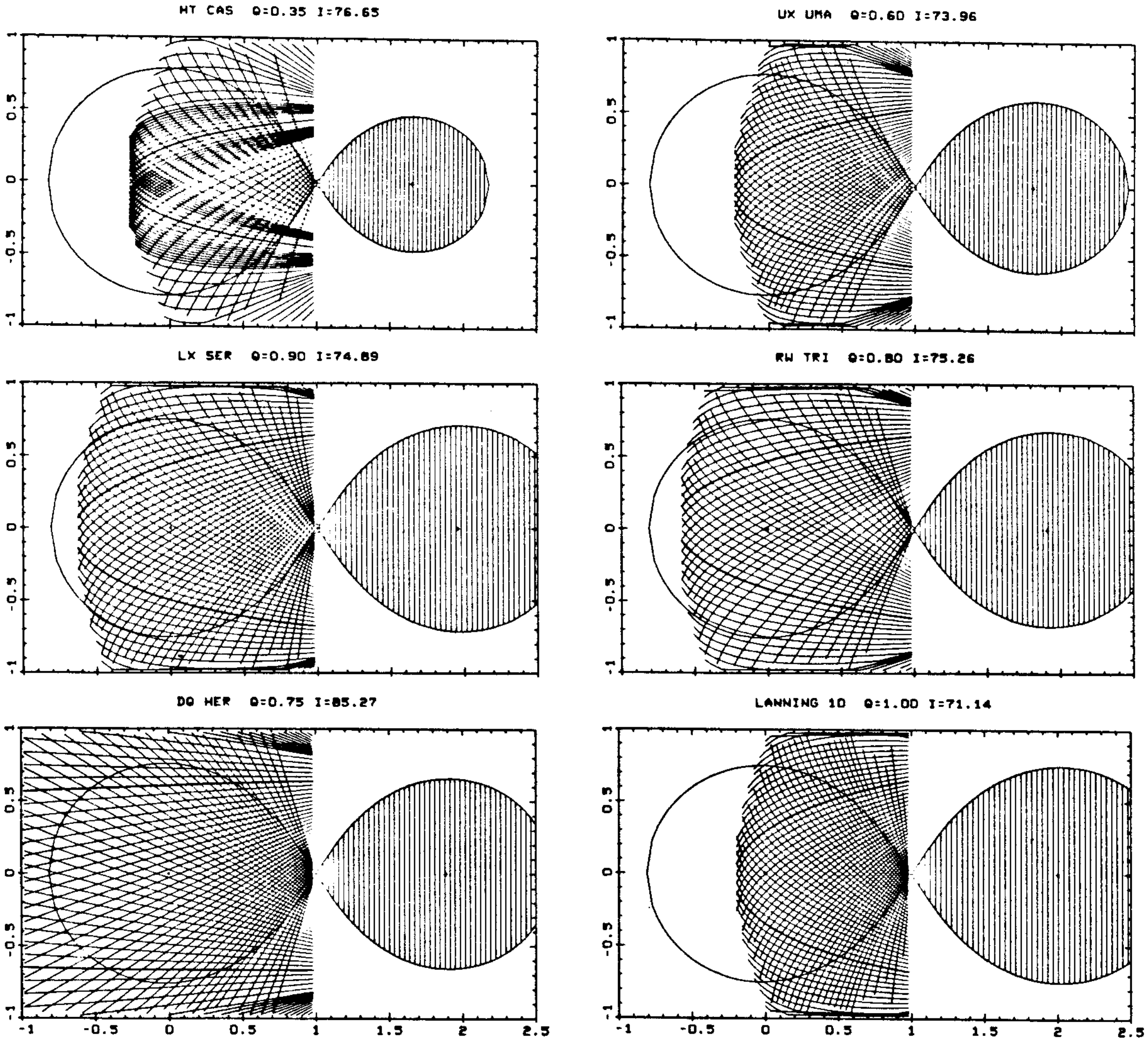

HT CAS Q=0.35 I=76.65

UX UMA Q=0.60 I=73.96

LX SER Q=0.90 I=74.89

RW TRI Q=0.80 I=75.26

DQ HER Q=0.75 I=85.27

LANNING 10 Q=1.00 I=71.14

Figure 6

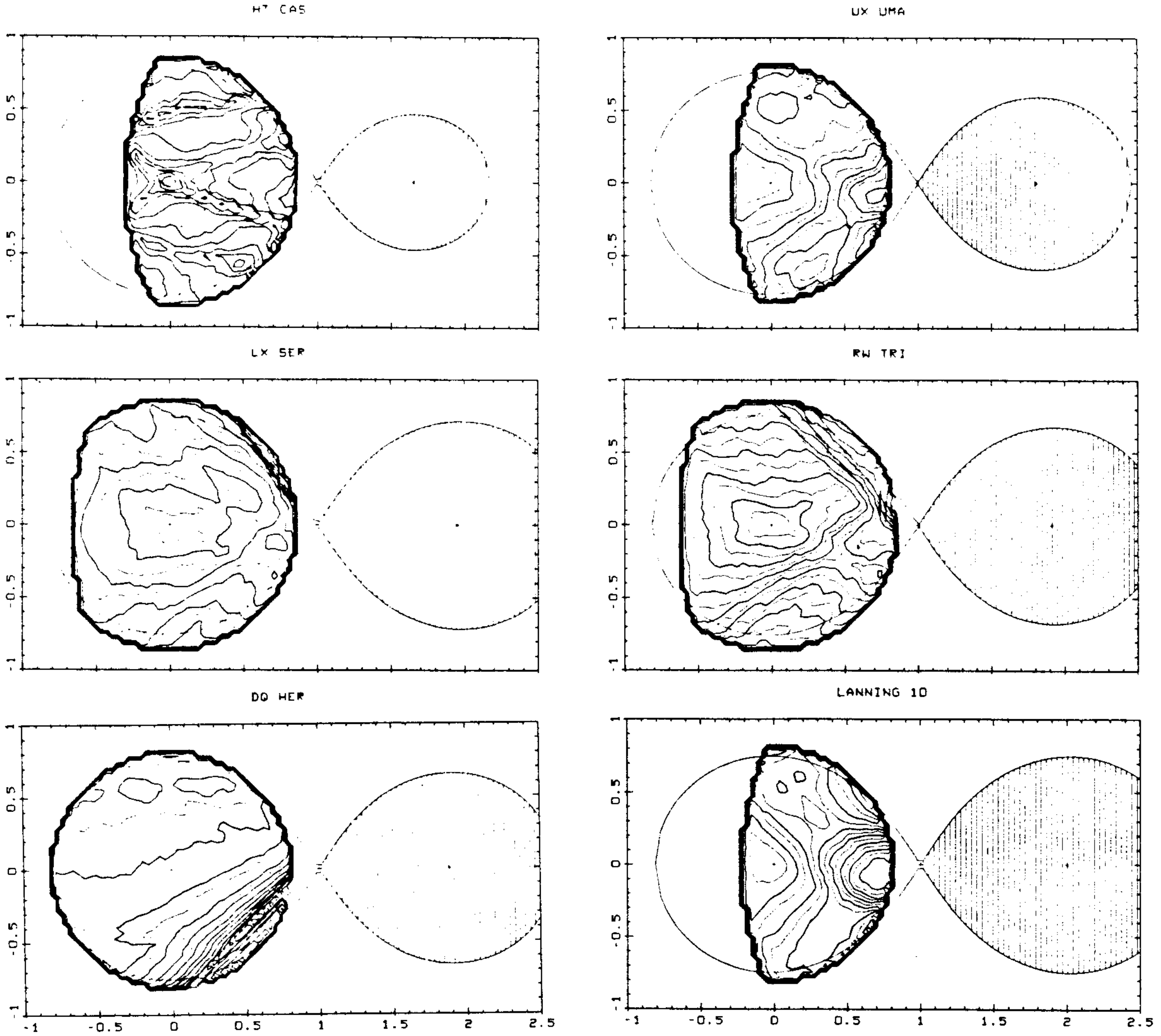

Figure 7

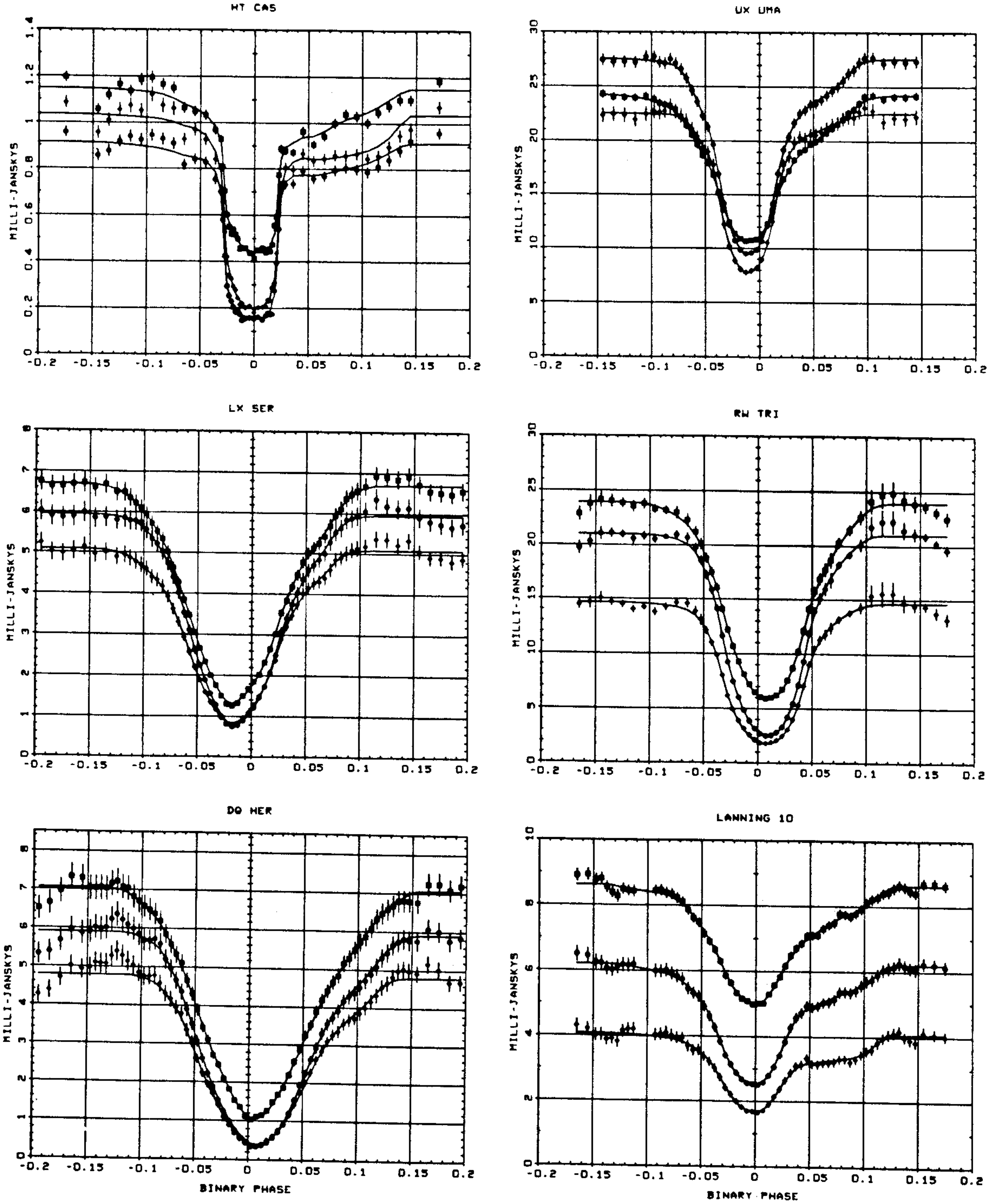
HT CAS
UX UMA
LX SER
RW TRI
DQ HER
LANNING 10
MILLI-JANSKYS
BINARY PHASE
-0.2
-0.15
-0.1
-0.05
0
0.05
0.1
0.15
0.2
0
0.2
0.4
0.6
0.8
1
1.2
1.4
5
10
15
20
25
30
1
2
3
4
5
6
7
8
2
4
6
8
10

Figure 8

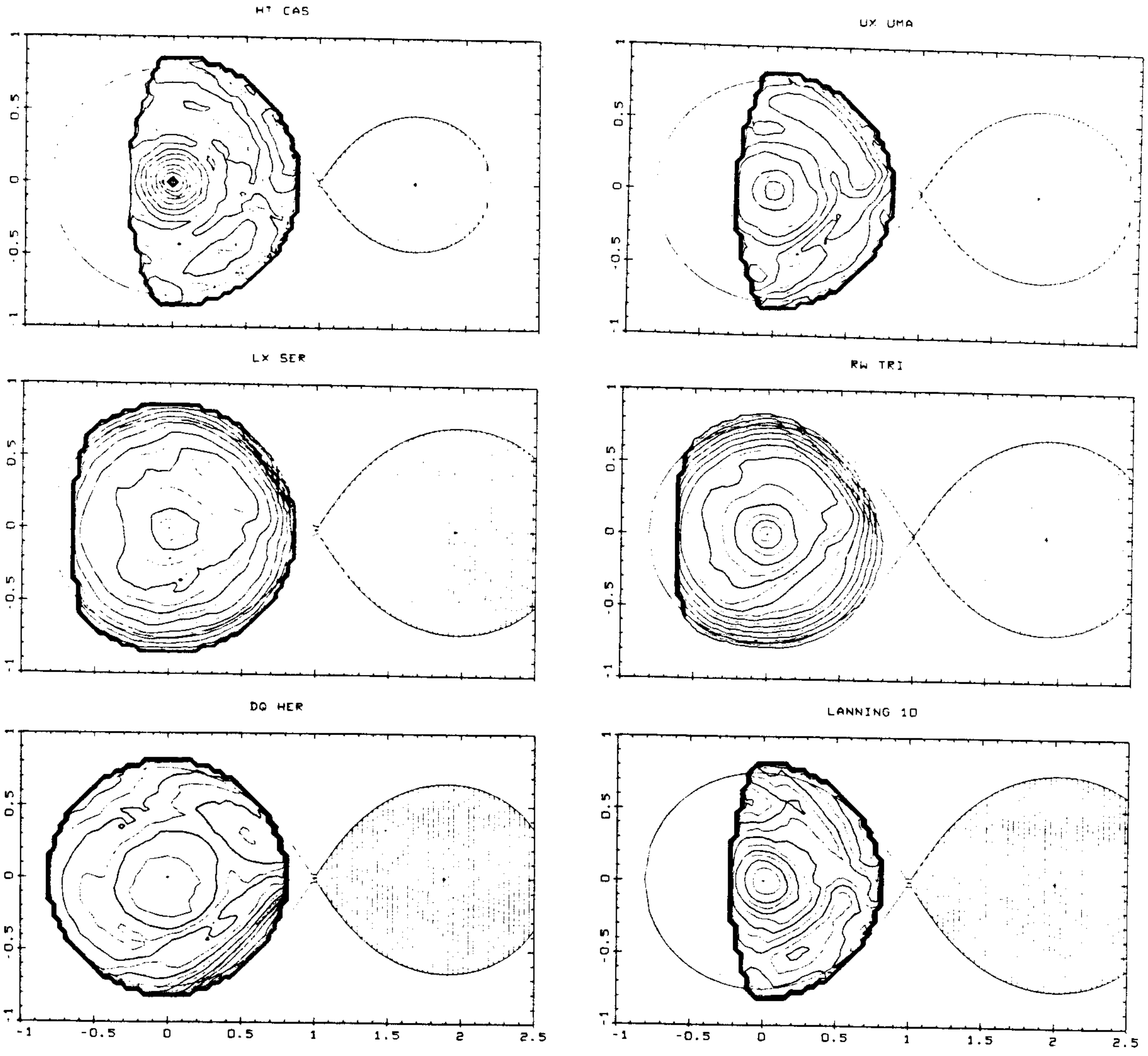
HT CAS
UX UMA
LX SER
RW TRI
DQ HER
LANNING 10
1
0.5
0
-0.5
-1
-1
-0.5
0
0.5
1
1.5
2
2.5

Figure 9

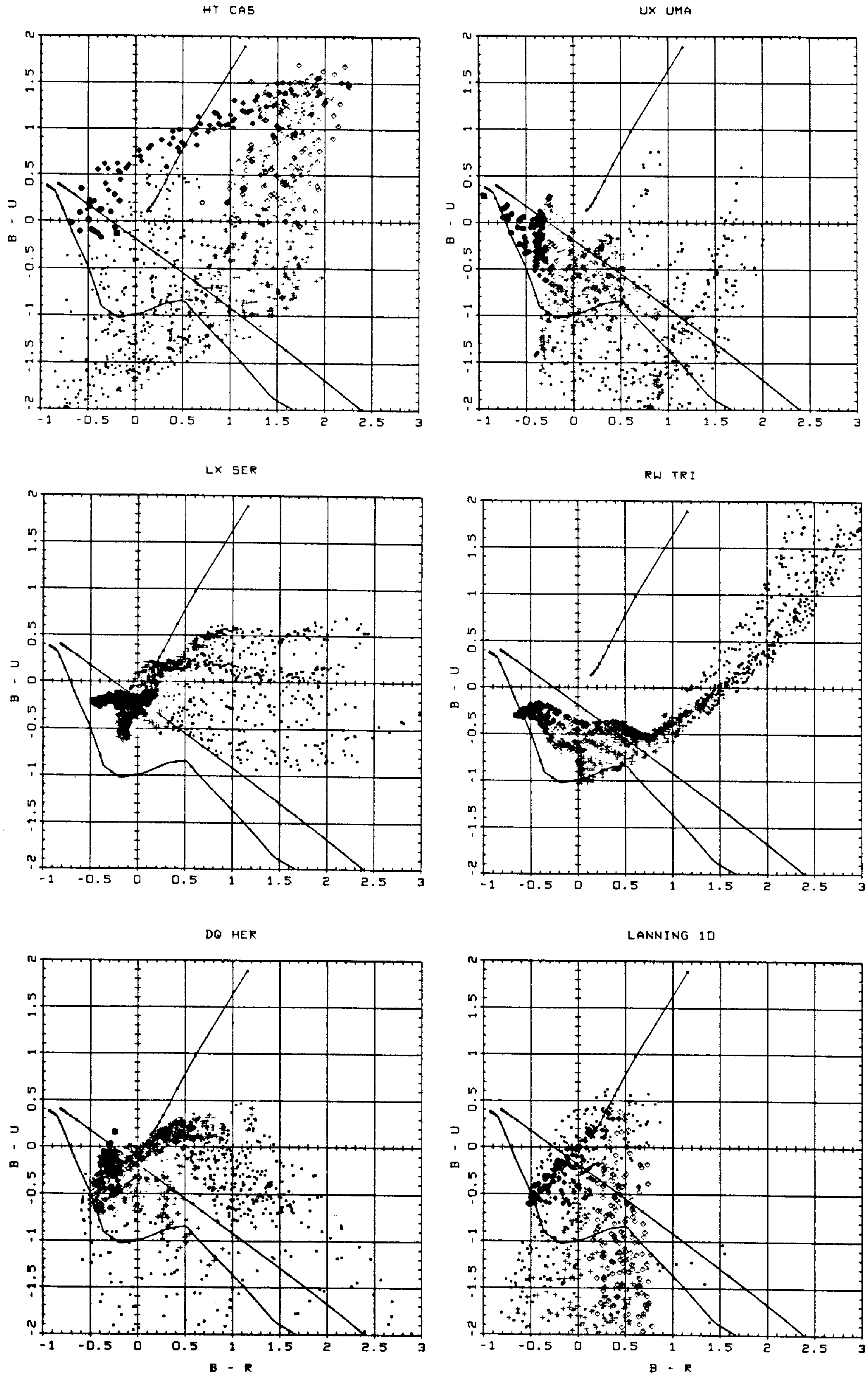
HT CAS
UX UMA
LX SER
RW TRI
DQ HER
LANNING 10
B - U
B - R
-1
-0.5
0
0.5
1
1.5
2
2.5
3
-2
-1.5
-1
-0.5
0
0.5
1
1.5
2

Figure 10

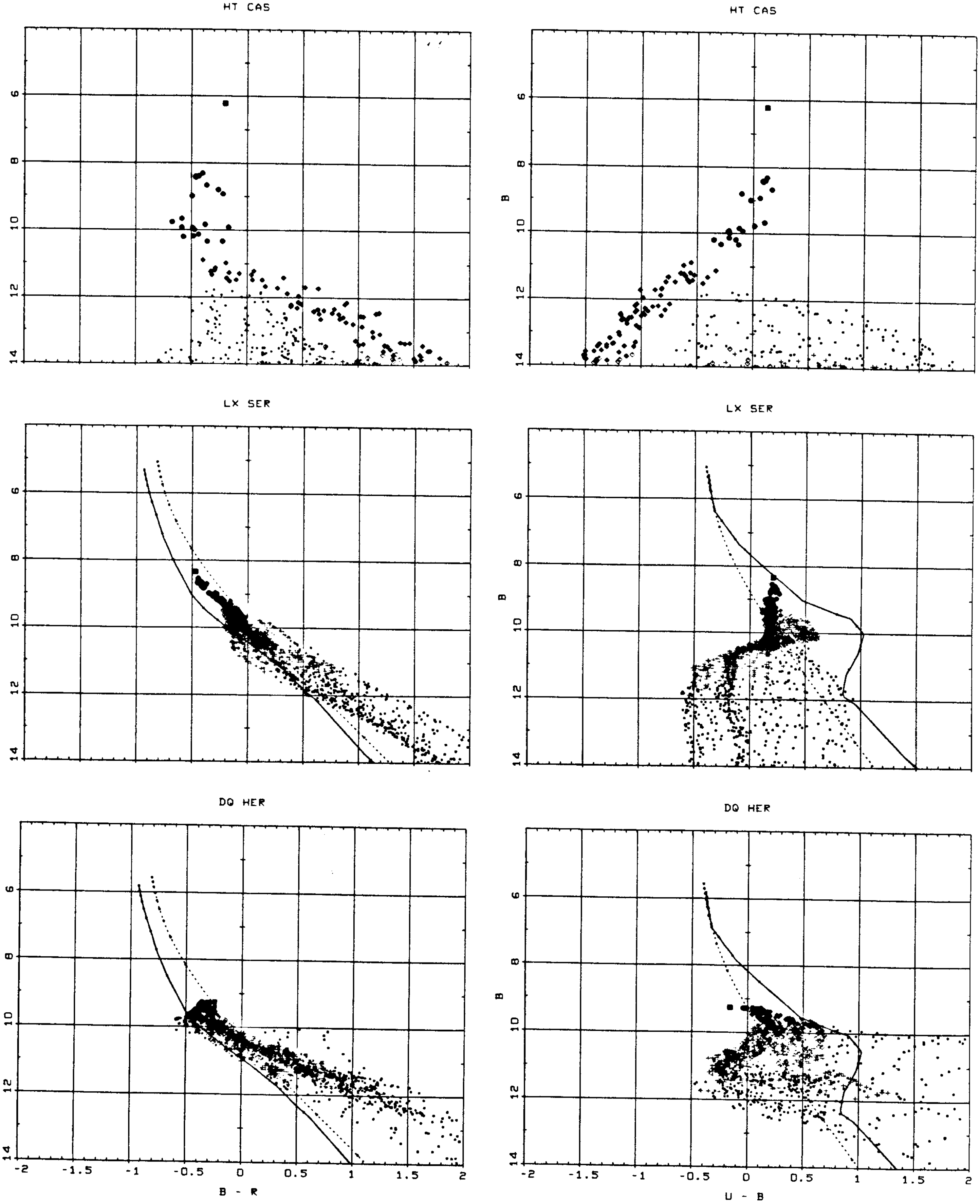
HT CAS
HT CAS
LX SER
LX SER
DQ HER
DQ HER
B
6
8
10
12
14
-2
-1.5
-1
-0.5
0
0.5
1
1.5
2
B - R
U - B

Figure 11a

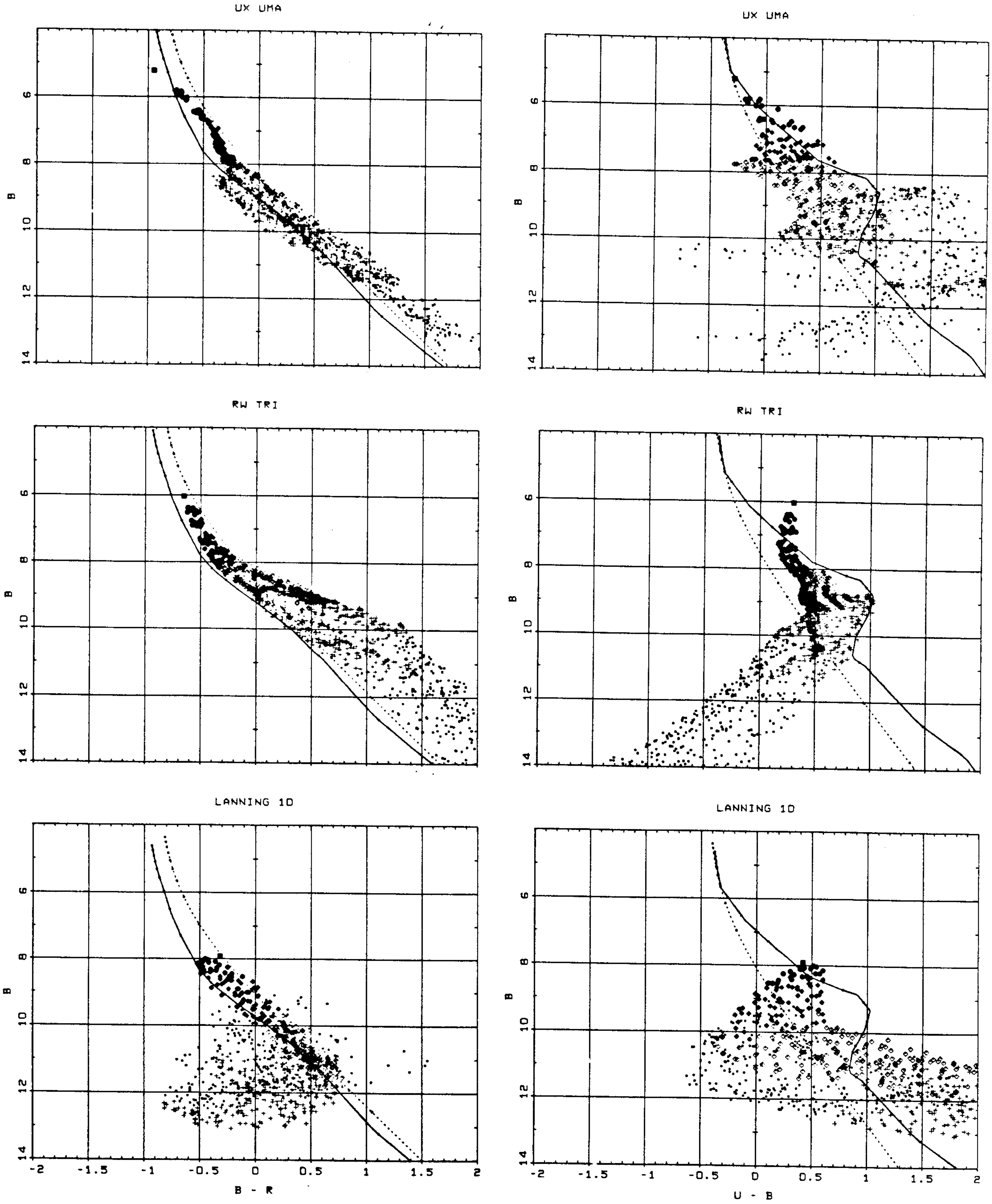
UX UMA
UX UMA
RW TRI
RW TRI
LANNING 10
LANNING 10
B
6
8
10
12
14
-2
-1.5
-1
-0.5
0
0.5
1
1.5
2
B - R
U - B

Figure 11b

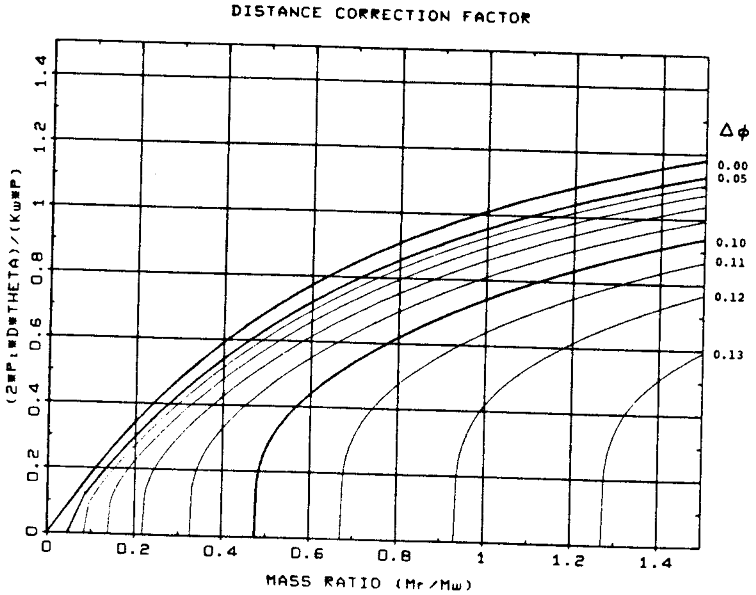
DISTANCE CORRECTION FACTOR
(2*PI*D*THETA)/(Kw*P)
0
0.2
0.4
0.6
0.8
1
1.2
1.4
MASS RATIO (Mr/Mw)
Δφ
0.00
0.05
0.10
0.11
0.12
0.13

Figure 12

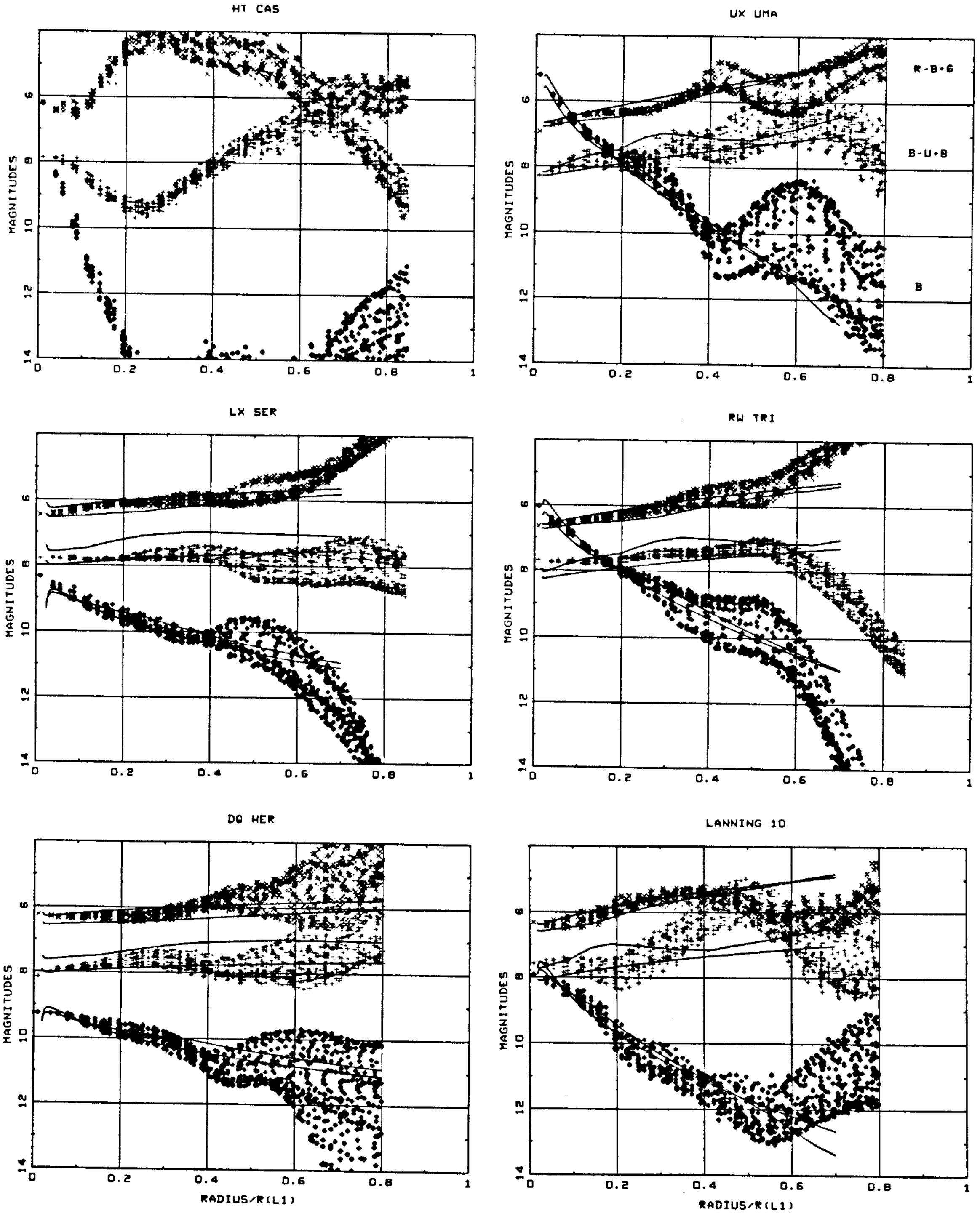
HT CAS
UX UMA
LX SER
RW TRI
DQ HER
LANNING 10
MAGNITUDES
6
8
10
12
14
0
0.2
0.4
0.6
0.8
1
R-B+6
B-U+8
B
RADIUS/R(L1)

Figure 13

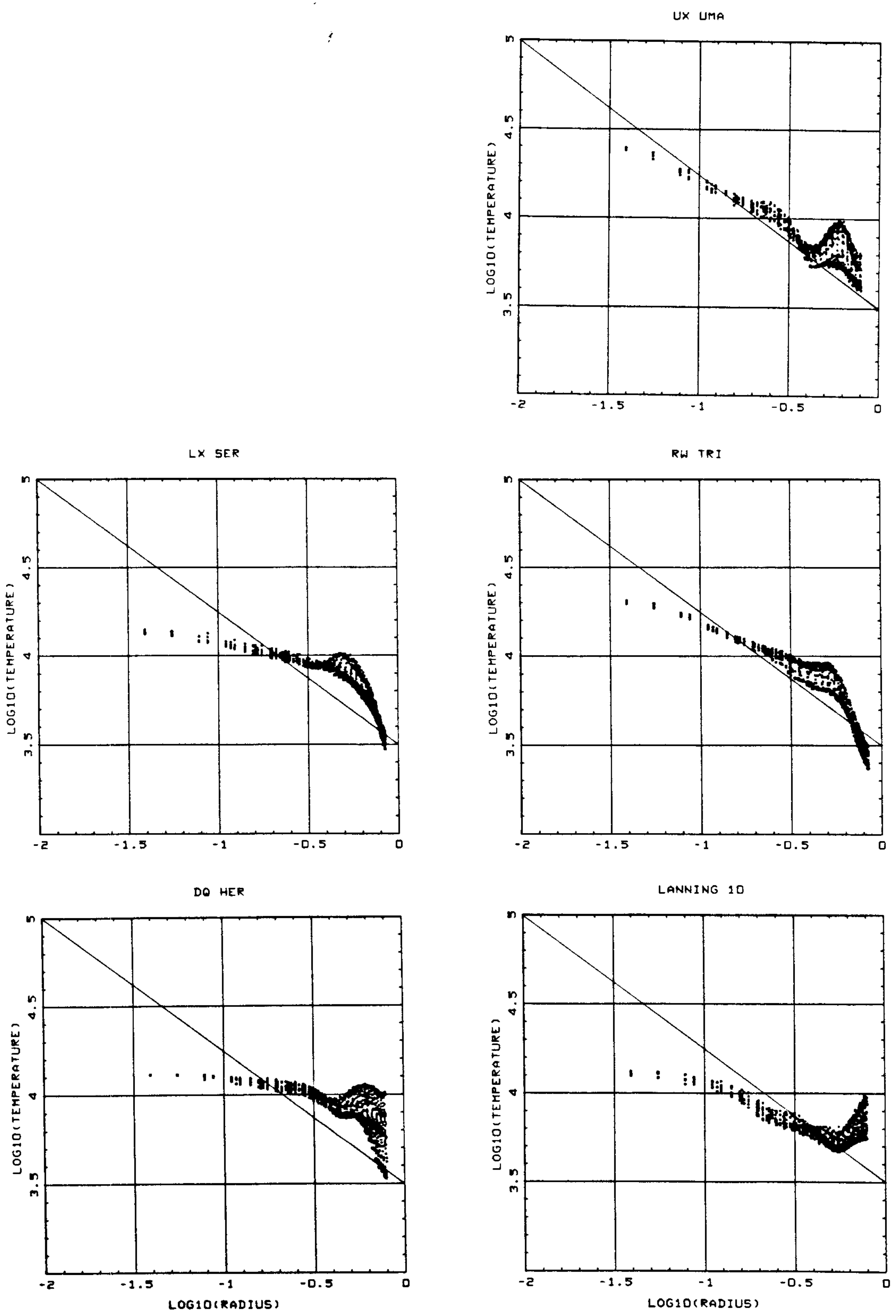
UX UMA
LX SER
RW TRI
DQ HER
LANNING 10
LOG10(TEMPERATURE)
LOG10(RADIUS)
5
4.5
4
3.5
-2
-1.5
-1
-0.5
0

Figure 14